Engineering Structures 195 (2019) 490–507

Contents lists available at ScienceDirect

Engineering Structures

journal homepage: www.elsevier.com/locate/engstruct

# Reliability of elastomeric-isolated buildings under historical earthquakes with/without forward-directivity effects

Hatice Gazi, Cenk Alhan*

*Department of Civil Engineering, İstanbul University – Cerrahpaşa, Avcılar Campus, 34320 Avcılar, İstanbul, Turkey*

ARTICLE INFO

*Keywords:*
Reliability analysis
Uncertainty
Monte Carlo simulation method
Seismic performance
Base isolation
Forward directivity effects
Near-fault earthquakes

ABSTRACT

Deviations from nominal design values of mechanical characteristics of seismic isolators are inevitable due to uncertainties and/or errors in material properties, element dimensions, construction methods, quality control, and/or installation steps, etc. In addition, due to uncertainties existing in active fault mechanisms affecting the site and local soil conditions, earthquake ground motions show record-to-record variability. Moreover, environmental conditions and/or time-dependent factors such as aging, temperature, and travel, etc. may also cause additional deviations in nominal values of characteristics of seismic isolators and thus in structural responses over the service life of structures. Therefore, in order to capture the dynamic behavior of base-isolated buildings realistically and design reliable base-isolated buildings, influence of such uncertainty should be taken into account. In this study, seismic reliability of realistic fully three-dimensional benchmark multi-story buildings equipped with nonlinear isolation systems is investigated under historical near-fault earthquakes. In order to take into account the uncertainties in the isolation system characteristics, pre-yield stiffness, post-yield stiffness, and yield displacement parameters are assumed as random variables, while the record-to-record variability nature of the ground motions is considered by using large sets of historical near-fault ground motions with or without forward-directivity effects. Two different levels of nominal isolation periods are taken into account while three different levels of uncertainty are considered for the random isolator characteristics. The reliability of the buildings is investigated in terms of structural integrity, isolation system safety, and the safety of the vibration-sensitive contents of the buildings using the peak bearing displacements and the peak floor accelerations obtained from the nonlinear time history analyses conducted in the framework of the Monte Carlo simulations. The plots including the average reliabilities for the displacement and the acceleration limit values provide a comprehensive picture in terms of the reliability level of the structural systems and of the vibration sensitive contents.

## 1. Introduction

Seismically isolated structures are generally mission-critical structures housing vibration-sensitive equipment which must go on serving even during an earthquake. However, such equipment may fail if floor accelerations sustained during such motions exceed certain limit values. In addition, the isolators may fail different failure modes [1] and endanger safety of the whole structure. Isolation system displacements may exceed the design limits for the base displacements and therefore cause buckling and/or rupture of isolators may occur [2]. Buckling is a specific concern for stability of elastomeric isolators when the critical axial load capacities of the isolators are exceeded along with the increases in the horizontal isolator displacements [3,4]. In such a case, the subject isolator displacements become unconstrained and increase freely [5]. In another failure mode, cavitation damages occur at a critical tensile stress value inside a rubber layer and gain importance for horizontal displacement levels corresponding to shear strains above 100% [6,7]. Finally shear failure could be observed at very high shear (i.e., on the order of approximately 300–500%) strain levels [4,8,1]. Above all these, in case one of the abovementioned failure modes occur in a significant number of isolators almost simultaneously, this may lead to the collapse of the whole isolation system [1]. Therefore, for obtaining reliable seismically isolated structural systems, it is economically and sometimes vitally important to determine the actual mechanical properties of isolation elements, which are used in the dynamic analyses of the subject systems, and take into account the factors that may lead to deviations in those mechanical characteristics. The effects of aging, temperature, scragging, travel, and/or heat, etc.

* Corresponding author.
*E-mail addresses:* hgazi@istanbul.edu.tr (H. Gazi), cenkalhan@istanbul.edu.tr (C. Alhan).

https://doi.org/10.1016/j.engstruct.2019.05.081
Received 23 January 2019; Received in revised form 28 April 2019; Accepted 25 May 2019
0141-0296/ © 2019 Elsevier Ltd. All rights reserved.

can be listed among the abovementioned factors which may threaten the safety of both the seismically isolated structure and its vibration-sensitive contents. Because, particularly the mechanical characteristics of seismic isolators vary over the service life of structures due to such effects and deviate from their nominal values, which are determined via extensive prototype tests [9]. Related research studies, including statistical data, can be found in Constantinou et al. [10], Kalpakidis et al. [11], and Cardone and Gesualdi [12]. In brief, as reported by Pan et al. [13], who reviewed the state-of-the-practice of design and construction of seismically isolated buildings in Japan where more than half of the seismically isolated structures around the world is located in [14], the mechanical characteristics of lead rubber bearings (LRBs) and high damping rubber bearings (HDRBs) vary from their nominal values, up to 20% and 25% due to the abovementioned factors respectively, while the lateral and vertical mechanical characteristics of low damping rubber bearings (LDRBs) are reported to vary up to 20% and 10% due to the same factors, respectively. Additionally, there are also inherent uncertainties in the mechanical characteristics of seismic isolators due to uncertainties and/or errors in their material properties, element dimensions, construction methods, quality control, and/or installation steps [15,16]. As one can predict, such deviations in the mechanical characteristics may trigger significant deviations in the structural responses from their nominal design values. Moreover, due to uncertainties existing in active fault mechanisms affecting the site and local soil conditions, earthquake ground motions show record-to-record variability. Therefore, for accurate analysis and design of seismically isolated structures, such uncertainties should be taken into account. Accordingly, stochastic response analyses and reliability analyses, considering inherent uncertainties, need to be conducted in evaluating the response of base-isolated structures comprehensively [17]. Consideration of uncertainties, which may lead to vulnerabilities in the structural systems and their nonstructural contents, is vital and should be taken into account via reliability analyses [18].

Most of the related previous studies take into account either the random nature of earthquake characteristics or the uncertainties in the isolation system, but not both. In such a study, Pradlwarter et al. [19] investigated the effects of deterministic two dimensional frictional devices on the structural reliability of a three-story building via the stochastic response analyses based on Monte Carlo simulations. Chen et al. [20] used a physical stochastic ground motion model and evaluated the reliability of a ten-story frame-shear wall hospital building equipped with a deterministic isolation system consisting of rubber-based bearings and viscous dampers. Using four sets of deterministic isolation systems and a set of various ground motion records, Morgan and Mahin [21] performed probabilistic seismic demand analyses for two multi-story shear-type buildings isolated by friction pendulum isolators and then computed the probability of satisfying some selected performance objectives for those buildings. Taflanidis and Jia [22] assessed the seismic risk occurrence probabilities for a planar base-isolated shear-frame using a simulation-based framework, which considers the uncertainties in the moment magnitude and the epicentral distance of the earthquake events but modeled the lead rubber bearings deterministically. Dang et al. [23] made a dynamic reliability evaluation for a seven-story building, which is mounted on a deterministic isolation system and subjected to Kanai-Tajimi spectrum, in terms of the interstory drift ratios.

There also exist studies that take into account the uncertainties in both the earthquake characteristics and the isolation system characteristics. But in these studies, either the seismic isolation systems are modeled linearly or the equivalent linear counterparts of the nonlinear isolation system elements are obtained via equivalent linearization techniques or the nonlinear-force deformation characteristics of the isolators are facilitated using stochastic linearization methods. In addition, the seismically isolated buildings are either represented by single or a few degree-of-freedom models or idealized as two dimensional shear frames. Pinto and Vanzi [24] took into account the uncertainties in the central frequency of the ground motion and the effective stiffness of the isolators for investigating the behavior of selected fractiles of peak displacements of a two-degree-of-freedom model with a linear isolation system. In order to compare the seismic reliabilities of a fixed-base and a seismically base-isolated reactor building, which were modeled as two and three-mass systems, respectively, Takeda et al. [25] demonstrated a probabilistic assessment method assuming the spectral acceleration of ground motion, the shear wave velocity of the site, the compressive strength of concrete, the elastic stiffness and ultimate deformation of rubber bearings, and the elastic stiffness of dampers as independent random variables. Alhan and Gavin [17] proposed a reliability-based method to determine the properties of high performance linear floor isolation systems taking into account both the uncertainties in the isolation system parameters and the ground motion characteristics. De Grandis et al. [26] proposed a numerical procedure to compute fragility functions for the equipment components of nuclear power plant reactor buildings under random excitation and validated the procedure via a linear single-degree-of-freedom base-isolated system. In order to calculate the fragility curves of bearing failure in isolated structures, Fan and Zhang [27] proposed a method which takes into account the uncertainties in the structural parameters including stiffness and damping of the linear rubber-based bearings and uses a probabilistic ground motion model which is based on adjusting the spectral accelerations of a group of selected real earthquake records. In another study, Castaldo et al. [28] presented reliability curves for a single-degree-of-freedom linear-shear type flexible steel building, which is isolated by frictional pendulum system and subjected to artificial ground motions. They took into account the friction coefficient of the isolators as random variable as well as the fundamental circular frequency and damping factor parameters of the soil strata included in the power spectral density function of the ground motion model. Castaldo et al. [29] derived the reliability curves for structural systems, which they modeled as two-degree-of-freedom systems consisting of inelastic superstructures mounted on bilinear friction pendulum isolators. They assumed the friction coefficient of the isolators as a random variable and took into account a set of natural seismic records in order to consider record-to-record variability of seismic excitations. And, Moeindarbari and Taghikhany [30] assumed the radius and the friction coefficient of the friction pendulum bearings and the artificially developed ground motion parameters as random variables; then assessed the seismic reliability of a two-dimensional three story concrete frame using artificial neural networks in comparison with Monte Carlo simulations.

Finally, to be distinct from the studies summarized above, a very recent comprehensive study presented by Cardone et al. [1] makes use of three dimensional reinforced concrete superstructures and isolation systems modeled nonlinearly for constructing fragility functions for existing reinforced concrete-frames representative of typical residential buildings built in Italy before 1970s and later retrofitted with base isolation technique. The record-to-record variability is quantified directly through incremental dynamic analysis while model variability was included via first order second moment approach. The effects of two sources of variability aforementioned above are then combined by the mean estimates method.

In this study, seismic reliability of buildings with elastomeric base-isolation systems under historical near-fault earthquakes is investigated using realistic full three-dimensional multi-story building models isolated with nonlinear isolation systems, and by taking into account both the uncertainties in the isolation system characteristics and the inherent record-to-record variabilities in the ground motion records. The uncertainties in the isolation system characteristics are taken into account by assuming pre-yield stiffness, post-yield stiffness, and yield displacement parameters as random variables while the inherent record-to-record variability nature of the ground motions is considered by using large sets of historical near-fault ground motions with or without forward-directivity effects. In order to represent the base-isolated

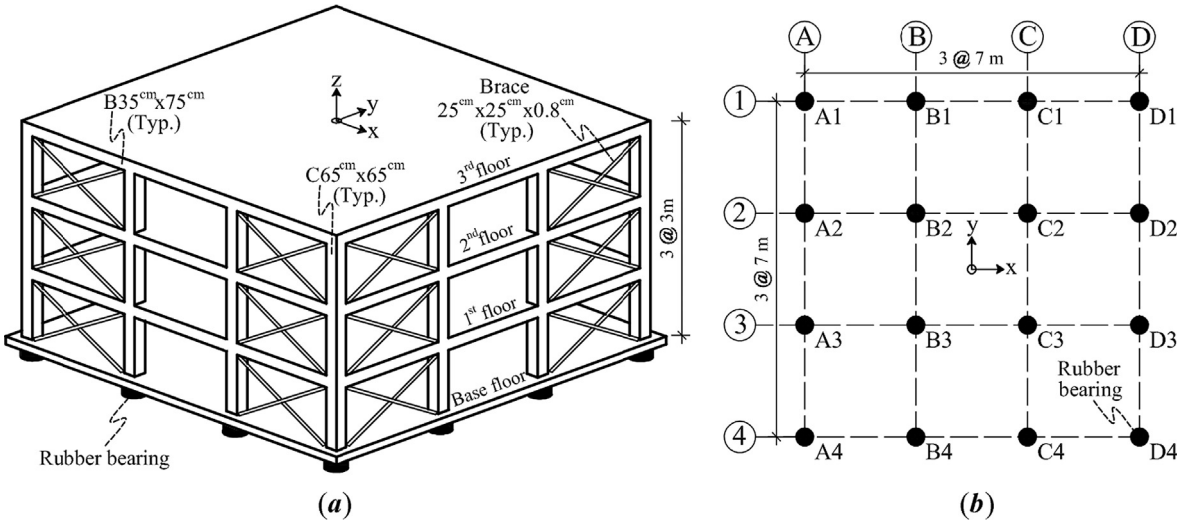


**Fig. 1.** (a) Three-dimensional view and (b) Isolation system plan of the benchmark building. adapted from [33]

buildings with short and relatively long periods, two different levels of nominal isolation periods are used while three different levels of uncertainty (i.e. coefficient of variation) are considered for the random isolator characteristics. The reliability of the buildings is investigated in terms of structural integrity, isolation system safety, and the safety of the vibration-sensitive contents of the buildings via Simulation Based Reliability Method consisting of Monte Carlo simulations; and is evaluated with respect to the closest fault distances, PGA/PGV ratios, pulse periods, and pulse amplitudes of the ground motion records. Bidirectional nonlinear time history analyses are conducted via a version of 3D-BASIS [31] modified by Gazi [32] to conduct recursive analyses in the framework of the Monte Carlo Simulation Method.

## 2. Mathematical model

Two full three-dimensional base isolated buildings, whose nominal isolation periods ($T_{0,nom}$) are 2.0 s and 3.5 s, are considered as benchmark buildings in this study. The subject buildings consist of two identical superstructures which are placed on two different nonlinear isolation systems. The three-dimensional views and the isolation system plans are shown in Fig. 1a and b, respectively. Along with the geometrical properties of the structural members of the superstructures and their associated material properties, the subject isolation system layouts are obtained from Tena-Colunga and Escamilla-Cruz [33]. The fixed-base periods of the first two modes, which are obtained from the free vibration analyses of these benchmark buildings carried out via SAP2000 [34], are both equal to 0.18 s which are the same as those reported by Tena-Colunga and Escamilla-Cruz [33].

### 2.1. Superstructure

The superstructure of the benchmark buildings has a square shaped typical floor plan consisting of three bays in x and y directions (Fig. 1). The structural system is composed of reinforced concrete ($f_c \approx 25$ N/mm$^2$, $E_c \approx 21{,}708$ N/mm$^2$) beams and columns and A36 steel braces which are located on the four corners of the superstructures. Each floor including the base floor has three degrees of freedom composed of two components of translation in the x and y directions and one component of rotation about the z axis. All floors including the base floor have equal translational (330 kNs$^2$/m) and rotational (24,280 kNs$^2$ m) masses lumped at their centers of mass. Superstructure modal damping ratio for each mode is taken as 3%. The moment resisting frames are modeled with rigid beam-to-column connections and the superstructure is assumed to remain elastic throughout the time history analyses.

### 2.2. Isolation systems

In this study, two main isolation systems whose nominal periods ($T_{0,nom}$) are 2.0 s and 3.5 s are considered. The subject isolation systems consist of 16 rubber-based bearings each of which is placed underneath each column (Fig. 1b). Nonlinear force-displacement characteristics and hysteretic energy dissipation behaviors are modeled via smooth inelastic bi-axial hysteretic model (Fig. 2, [35]), which is characterized by the pre-yield stiffness ($K_1$), the post-yield stiffness ($K_2$), the characteristic force ($Q$), the yield force ($F_y$), and the yield displacement ($D_y$) of the isolators. Although the general layouts of the isolation systems are identical to Tena-Colunga and Escamilla-Cruz [33] as explained above, the characteristic parameters of the isolators are modeled as random variables in the context of the Monte Carlo Simulation Method in this study and thus are different from Tena-Colunga and Escamilla-Cruz [33] as explained below.

The nominal values of the abovementioned characteristic parameters and the stiffness ratios ($\alpha$=$K_2/K_1$) considered for the isolation systems are listed in Table 1. In this table, the nominal values of the post-yield stiffness ($K_2$) of the isolators are obtained using Eq. (1), where $T_0$ is the rigid-body mode period, $M$ is the total translational mass (1320 kNs$^2$/m) of the base-isolated building, and $n_b$ is the total number of bearings in the isolation system. As reported in the research studies published towards the end of 1990s (e.g. [36]), isolation periods of most base-isolated buildings were within a range between 2.0 s and 3.0 s. However, in parallel to increase in sizes and capacities of isolation system elements, fundamental periods of seismically isolated buildings

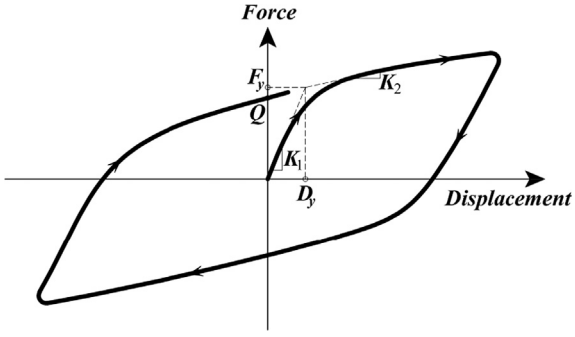


**Fig. 2.** Force-displacement relationship of the isolators.

**Table 1**
Nominal values of the isolator characteristic parameters.

| Benchmark isolation system (BIS) | Isolator characteristic parameter | | | | | |
|---|---|---|---|---|---|---|
| | $K_1$ (kN/m) | $K_2$ (kN/m) | $Q$ (kN) | $D_y$ (mm) | $F_y$ (kN) | $\alpha$ (–) |
| **1st BIS ($T_{0,nom}$) = 2.0 s** | 8150.65 | 815.06 | 40.51 | 5.52 | 45.01 | 0.10 |
| **2nd BIS ($T_{0,nom}$) = 3.5 s** | 2661.44 | 266.14 | 40.51 | 16.91 | 45.01 | 0.10 |

have also increased. According to a report by Building Center of Japan [37]; the equivalent periods of the most (37%) of the base isolated structures in Japan are between 3.0 s and 3.5 s, while the equivalent periods of 23% and 21% of those are in the ranges of 2.5–3.0 s and 3.5–4.0 s, respectively. Therefore, in order to cover a wide range to include isolation periods preferred for most of the base-isolated buildings, nominal rigid-body mode periods ($T_{0,nom}$) of the benchmark-isolated buildings are assumed as 2.0 s and 3.5 s in this study.

$$K_2 = (4\pi^2 M)/(n_b T_0^2) \quad (1)$$

The pre-yield stiffness ($K_1$) values of LRBs, reported in many technical documents and research studies [38,9,39], range between 6.5 and 16 times the post-yield stiffness ($K_2$) of the isolators. In addition, pre-yield stiffness of HDRBs are reported to be as 10 times their post-yield stiffness [40]. Compatible with the abovementioned values, the nominal stiffness ratios ($\alpha$) of the benchmark isolation systems are taken as 0.10 as a typical average value and the nominal pre-yield stiffness ($K_1$) values of the isolators, given in Table 1, are calculated accordingly.

The nominal characteristic strengths ($Q$) of the isolators are calculated based on the target ranges determined for the total characteristic strength ratios ($Q_{total}/W$) of the isolation systems. The total characteristic strength ratio ($Q_{total}/W = n_b \times Q/W$) determines the strength of an isolation system with respect to the total structure weight [41]. Many research studies in the literature (e.g. [41–43]) consider values for $Q_{total}/W$ in 3% to 10% range. The nominal total characteristic strength ratios ($Q_{total}/W$) of the benchmark isolation systems, which are assumed as 5% in this study, fall in the aforementioned range.

Following the calculation of nominal values for $Q$, nominal yield displacements ($D_y$) of the benchmark isolation systems are obtained via Eq. (2) [44] based on the parameters $Q$, $K_1$ and $K_2$. As stated by ASCE/SEI 41-13 [38], $D_y$ can be approximately considered in the range between 0.05 and 0.10 times the total rubber thickness according to the experimental data obtained from the tests applied for the bearings. According to the seismic isolation product catalogues provided by the manufacturers [45,40], typical range of $D_y$ is 5–30 mm. The values considered in this study for $D_y$ (i.e. 5.5 mm and are 16.9 mm, See Table 1) are in this range. Subsequently, the nominal yield strengths ($F_y$) of the isolators are calculated based on the nominal values of the yield displacement and the nominal pre-yield stiffness parameters as given in Eq. (3) [44].

$$D_y = Q/(K_1 - K_2) \quad (2)$$

$$F_y = K_1 \times D_y \quad (3)$$

### 2.3. Generation of random variables and probabilistic distributions

In order to obtain the probability of failures and reliability statistics for the base-isolated buildings taking into account the uncertainties in the isolation system parameters and record-to-record variabilities in the earthquake ground motions, Monte Carlo Simulation Method is employed in this study. Monte Carlo is a simulation method which makes use of statistical sampling experiments in order to solve complex problems without conducting any physical testing [46]. There are a large number of studies using this method in conducting probability, sensitivity, risk, etc. analyses in physics (e.g. [47]), engineering (e.g. [48]), finance (e.g. [49]), and telecommunication (e.g. [50]) problems. This method can be used as a very effective tool in solving various complicated structural reliability problems conveniently and with a reasonable approximation to analytical solutions [17]. In the context of the Monte Carlo Simulation Method, the problem is defined in terms of all random variables at first. Subsequently, the values of the random variables are generated following a specified probabilistic distribution by making use of their nominal values and coefficients of variation. Then, the problem is solved for each realization of the values of the random variables generated. Finally, statistical information is extracted from all simulated cases [51].

In order to take into account the uncertainties in the isolation system characteristics here, $K_1$, $K_2$, and $D_y$ parameters of the isolators are modeled as random variables ($X$) following normal distribution using Eq. (4) [51]. Normal distribution is among the mostly used statistical distributions for structural reliability problems in engineering and the probability density function (pdf, $f_X$) of a normally distributed random variable, which indicates the random characteristic of that variable, can be expressed by Eq. (5) [46]. In these equations, $\mu_X$ and $COV_X$ are the mean and the coefficient of variation of the random variable $X$, respectively, whose standard deviation ($\sigma_X$) is calculated by $\sigma_X = COV_X \times \mu_X$, while $x_i$ represents a particular realization of that variable. In addition, $s_i$ corresponds to standard normal random numbers with zero mean ($\mu = 0$) and unit standard deviation ($\sigma = 1$), which are obtained via the inverse cumulative distribution function method as the transformation of the uniform random numbers between 0 and 1.

$$x_i = \mu_X + (COV_X \times \mu_X)s_i \quad (4)$$

$$f_X(x) = \frac{1}{(COV_X \times \mu_X)\sqrt{2\pi}} e^{-(x-\mu_X)^2/2(COV_X \times \mu_X)^2} \quad (5)$$

The mean values of the abovementioned normally distributed random variables are considered to be equal to the nominal values given in Table 1. $COV_X$ values of those variables, which indicate the level of their uncertainties or randomness [51] are assumed as 5%, 10%, and 15% corresponding to the three levels of uncertainty considered for the random parameters of each of the benchmark isolation systems. Thus, a total of six subsets of benchmark isolation systems are considered: The first three subsets are generated based on the 1st benchmark isolation system and the second three subsets are generated

**Table 2**
Properties of the subsets of the benchmark isolation systems.

| Benchmark isolation system | Isolation system subsets | Nominal period $T_{0,nom}$ (s) | Coefficient of variation ($COV$) (%) | Benchmark isolation system | Subset | Nominal period $T_{0,nom}$ (s) | Coefficient of variation ($COV$) (%) |
|---|---|---|---|---|---|---|---|
| **1st BIS** | T20COV05 | 2.0 | 5 | **2nd BIS** | T35COV05 | 3.5 | 5 |
| | T20COV10 | | 10 | | T35COV10 | | 10 |
| | T20COV15 | | 15 | | T35COV15 | | 15 |

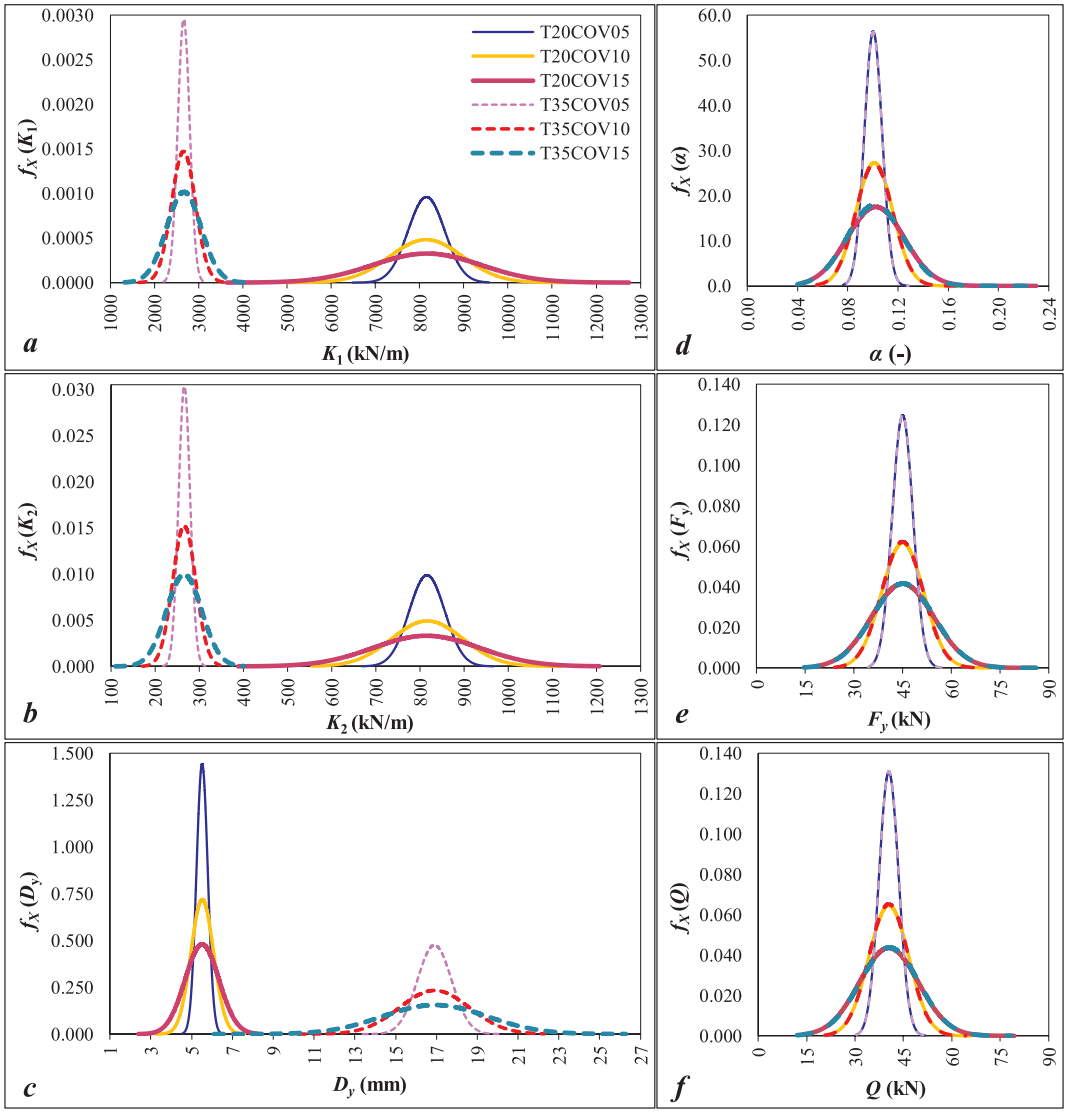


**Fig. 3.** Probability Density Function (PDF) plots of characteristic isolator parameters for the representative case of isolator A4.

based on the 2nd benchmark isolation system as shown in Table 2.

The characteristic parameters ($\alpha$, $F_y$, and $Q$) of the isolators of these subsets are generated to follow the relationships given in Section 2.2. The probability density function ($f_X$) plots for all isolator characteristic parameters ($K_1$, $K_2$, $D_y$, $\alpha$, $F_y$, and $Q$) of a representative isolator (A4) for all isolation system subsets are given in Fig. 3. It should be noted here that, 5000 different values are generated for each of the above-mentioned characteristic parameters of each isolator in each benchmark isolation system for conducting Monte Carlo simulations. The adequacy of the number of Monte Carlo simulations, $N_{MCS}$ = 5000, is verified via an initial simulation study, which is based on the convergence of probabilities of exceeding different limit state values determined for different response parameters of the benchmark buildings [32].

## 3. Ground motion records

The ground motions at a site in close proximity to a fault rupture are generally affected by the rupture mechanism and the slip direction [52] and often involve long period pulses with high velocities on their horizontal strike-normal components due to the forward rupture directivity effects [53]. The pulse-like ground motions resulting from forward rupture directivity effects may cause more hazardous seismic demands particularly in base-isolated buildings than those with the same *PGA* values and duration of shaking but without directivity pulses [54]. Therefore, the effects of those type of ground motions on the base-isolated buildings located in the near-fault zones must be taken into account while designing such structures [55].

Thus, 108 near-fault ground motion records with and without forward directivity effects from the 1999 Chi-Chi Earthquake (Taiwan), the 1999 Kocaeli Earthquake (Turkey), the 1999 Düzce Earthquake (Turkey), the 1989 Loma Prieta Earthquake (USA), the 1994 Northridge Earthquake (USA), and the 1992 Erzincan Earthquake (Turkey) are used in this study. The moment magnitudes of these 6 historical earthquakes vary in the range of 6.70–7.60, and all ground motion records are taken from 54 stations in close proximity (between 0.24 km and 24.00 km) to the fault ruptures. The list of the ground motion components which are applied to the buildings in the x-direction has been obtained from Sehhati et al. [55] and the properties of those components, including their closest distances to the faults ($r$), peak ground accelerations (*PGA*), peak ground velocities (*PGV*), peak ground displacements (*PGD*), and pulse periods ($T_p$) are given in Table 3. In order to investigate the differences in the probabilistic seismic behavior of the base-isolated buildings based on the ground motion characteristics, the loading cases are divided into two groups as seen in this table: those with forward-directivity effects are listed with FDi (i = 1–27)

**Table 3**
Ground motion components applied in the x-direction.
adapted from [55]

| Loading code* | Earthquake | Station | | x-Component | | | | |
|---|---|---|---|---|---|---|---|---|
| | | Name | *r* (km) | Name | *PGA* (g) | *PGV* (cm/s) | *PGD* (cm) | $T_p$ (s) |
| FD1 | 1999 Chi-Chi | TCU052 | 0.24 | TCU052-W | 0.348 | 159.00 | 184.50 | 6.12 |
| FD2 | 1999 Chi-Chi | TCU068 | 1.09 | TCU068-N | 0.462 | 263.10 | 430.20 | 4.25 |
| FD3 | 1999 Chi-Chi | TCU075 | 1.49 | TCU075-W | 0.333 | 88.30 | 86.50 | 2.41 |
| FD4 | 1999 Chi-Chi | TCU101 | 2.94 | TCU101-W | 0.202 | 67.90 | 75.40 | 6.86 |
| FD5 | 1999 Chi-Chi | TCU102 | 1.79 | TCU102-W | 0.298 | 112.50 | 89.20 | 9.11 |
| FD6 | 1999 Kocaeli | Düzce | 12.70 | DZC180 | 0.312 | 58.90 | 44.10 | 1.36 |
| FD7 | 1999 Kocaeli | Arçelik-Kandilli | 17.00 | ARC090 | 0.150 | 39.60 | 35.60 | 7.97 |
| FD8 | 1999 Kocaeli | Gebze | 17.00 | GBZ000 | 0.244 | 50.30 | 42.80 | 5.97 |
| FD9 | 1989 Loma Prieta | Gilroy-Gavilan Coll. | 11.60 | GIL067 | 0.357 | 28.60 | 6.40 | 1.80 |
| FD10 | 1989 Loma Prieta | Gilroy-Historic Bldg. | 12.70 | GOF090 | 0.284 | 42.00 | 11.10 | 1.80 |
| FD11 | 1989 Loma Prieta | Gilroy Array#1 | 11.20 | GO1090 | 0.473 | 33.90 | 8.05 | 4.31 |
| FD12 | 1989 Loma Prieta | Gilroy Array#2 | 12.70 | GO2090 | 0.322 | 39.10 | 12.10 | 1.72 |
| FD13 | 1989 Loma Prieta | Gilroy Array#3 | 14.40 | GO3090 | 0.367 | 44.70 | 19.30 | 2.32 |
| FD14 | 1989 Loma Prieta | LGPC | 6.10 | LGP000 | 0.563 | 94.80 | 41.10 | 3.92 |
| FD15 | 1989 Loma Prieta | Saratoga-Aloha Ave. | 13.00 | STG090 | 0.324 | 42.60 | 27.60 | 4.47 |
| FD16 | 1989 Loma Prieta | Saratoga- W Valley Coll. | 13.70 | WVC270 | 0.332 | 61.50 | 36.30 | 1.90 |
| FD17 | 1994 Northridge | Jensen Filter Plant | 6.20 | JEN022 | 0.424 | 106.20 | 43.20 | 3.36 |
| FD18 | 1994 Northridge | Newhall-Fire Sta. | 7.10 | NWH360 | 0.590 | 96.90 | 38.20 | 1.04 |
| FD19 | 1994 Northridge | Newhall-W. Pico Can. Rd. | 7.10 | WPI046 | 0.455 | 92.80 | 56.60 | 2.41 |
| FD20 | 1994 Northridge | Rinaldi Receiving Sta. | 7.10 | RRS228 | 0.838 | 166.10 | 28.20 | 1.50 |
| FD21 | 1994 Northridge | Sylmar-Converter Sta. | 6.20 | SCS052 | 0.612 | 117.40 | 54.30 | 3.48 |
| FD22 | 1994 Northridge | Sylmar-Converter Sta. E. | 6.10 | SCE018 | 0.828 | 117.50 | 34.50 | 3.49 |
| FD23 | 1994 Northridge | Sylmar-Olive View FF | 6.40 | SYL360 | 0.843 | 129.40 | 31.90 | 3.11 |
| FD24 | 1994 Northridge | Pacoima Kagel Canyon | 8.20 | PKC360 | 0.433 | 51.20 | 8.00 | 0.90 |
| FD25 | 1994 Northridge | Arleta-Nordhoff Fire Sta. | 9.20 | ARL090 | 0.344 | 40.60 | 15.10 | 1.23 |
| FD26 | 1994 Northridge | Pacoima Dam (downstr.) | 8.00 | PAC175 | 0.415 | 45.60 | 5.00 | 0.59 |
| FD27 | 1992 Erzincan | Erzincan | 2.00 | ERZ-NS | 0.515 | 83.90 | 27.66 | 2.65 |
| NFD1 | 1999 Chi-Chi | CHY028 | 7.31 | CHY028-N | 0.821 | 67.00 | 23.30 | – |
| NFD2 | 1999 Chi-Chi | CHY029 | 15.28 | CHY029-W | 0.277 | 30.30 | 14.70 | – |
| NFD3 | 1999 Chi-Chi | CHY035 | 18.12 | CHY035-W | 0.252 | 45.60 | 12.00 | – |
| NFD4 | 1999 Chi-Chi | CHY080 | 6.95 | CHY080-W | 0.968 | 107.60 | 18.60 | – |
| NFD5 | 1999 Chi-Chi | CHY006 | 14.93 | CHY006-E | 0.364 | 55.40 | 25.60 | – |
| NFD6 | 1999 Chi-Chi | TCU055 | 6.88 | TCU055-W | 0.237 | 26.20 | 10.00 | – |
| NFD7 | 1999 Chi-Chi | TCU070 | 19.10 | TCU070-W | 0.255 | 52.20 | 48.10 | – |
| NFD8 | 1999 Chi-Chi | TCU071 | 4.94 | TCU071-N | 0.655 | 69.40 | 49.10 | – |
| NFD9 | 1999 Chi-Chi | TCU072 | 7.36 | TCU072-W | 0.489 | 71.80 | 38.70 | – |
| NFD10 | 1999 Chi-Chi | TCU074 | 13.67 | TCU074-W | 0.597 | 73.40 | 20.50 | – |
| NFD11 | 1999 Chi-Chi | TCU079 | 10.04 | TCU079-W | 0.743 | 61.20 | 11.10 | – |
| NFD12 | 1999 Chi-Chi | TCU089 | 8.22 | TCU089-W | 0.333 | 30.90 | 18.50 | – |
| NFD13 | 1999 Düzce | Bolu | 17.60 | BOL-090 | 0.822 | 62.10 | 13.60 | – |
| NFD14 | 1999 Düzce | Düzce | 8.20 | DZC-270 | 0.535 | 83.50 | 51.60 | – |
| NFD15 | 1989 Loma Prieta | BRAN | 10.30 | BRN-090 | 0.501 | 44.60 | 4.90 | – |
| NFD16 | 1989 Loma Prieta | Capitola | 14.50 | CAP-000 | 0.529 | 36.50 | 9.10 | – |
| NFD17 | 1989 Loma Prieta | Corralitos | 5.10 | CLS-000 | 0.644 | 55.10 | 10.80 | – |
| NFD18 | 1989 Loma Prieta | UCSC Lick Observatory | 17.90 | LOB-000 | 0.450 | 18.70 | 3.80 | – |
| NFD19 | 1989 Loma Prieta | UCSC | 18.10 | UC2-090 | 0.396 | 13.20 | 2.30 | – |
| NFD20 | 1989 Loma Prieta | WAHO | 16.90 | WAH-090 | 0.638 | 37.90 | 5.90 | – |
| NFD21 | 1994 Northridge | N Hollywood-Coldwater Can. | 14.60 | CWC-180 | 0.298 | 25.00 | 6.30 | – |
| NFD22 | 1994 Northridge | Sunland-Mt Gleason Ave. | 17.70 | GLE-260 | 0.157 | 14.50 | 4.40 | – |
| NFD23 | 1994 Northridge | Burbank-Howard Rd. | 20.00 | HOW-330 | 0.163 | 8.50 | 1.80 | – |
| NFD24 | 1994 Northridge | Simi-Valley-Katherine Rd. | 14.60 | KAT-000 | 0.877 | 40.90 | 5.30 | – |
| NFD25 | 1994 Northridge | Sun Valley-Roscoe Blvd. | 12.30 | RO3-090 | 0.443 | 38.20 | 10.10 | – |
| NFD26 | 1994 Northridge | Santa Susana Ground | 19.30 | SSU-090 | 0.290 | 19.50 | 7.70 | – |
| NFD27 | 1994 Northridge | Big Tujunga, Angeles Nat F. | 24.00 | TUJ-352 | 0.245 | 12.70 | 1.10 | – |

*FD: Forward Directivity.
* NFD: Non-Forward Directivity.

codes, while those with no forward-directivity effects are listed with NFDi (i = 1–27) codes.

It should be stated here that, it would be preferable to take into account as many ground motion histories as possible in order to evaluate the record-to-record variability nature of the ground motions better. However, Monte Carlo Simulation Method that was used in this study is an extremely numerical-intensive method which takes very long computing time particularly when nonlinear models are considered. Therefore, we chose to use a feasible number of ground motion loadings consisting of 27 FD and 27 NFD loadings (i.e. a total of 54 ground motion couples) that is also compatible with the number of ground motions used in other related studies carried out in similar study areas in the literature (e.g. [28,29,56,57]).

The 10% damped response spectra including the spectral accelerations and the spectral displacements for the subject components (FD and NFD) are given in Fig. 4. It should be noted here that, the buildings are subjected to the bidirectional loadings applied in the x and y directions. However, due to the limited space, the results of the bidirectional analyses in the x direction are presented in this paper. Accordingly, only the list of the ground motion components applied in the x-direction is given here. All acceleration records used, including the ones perpendicular to those in Table 3, are obtained from the database of

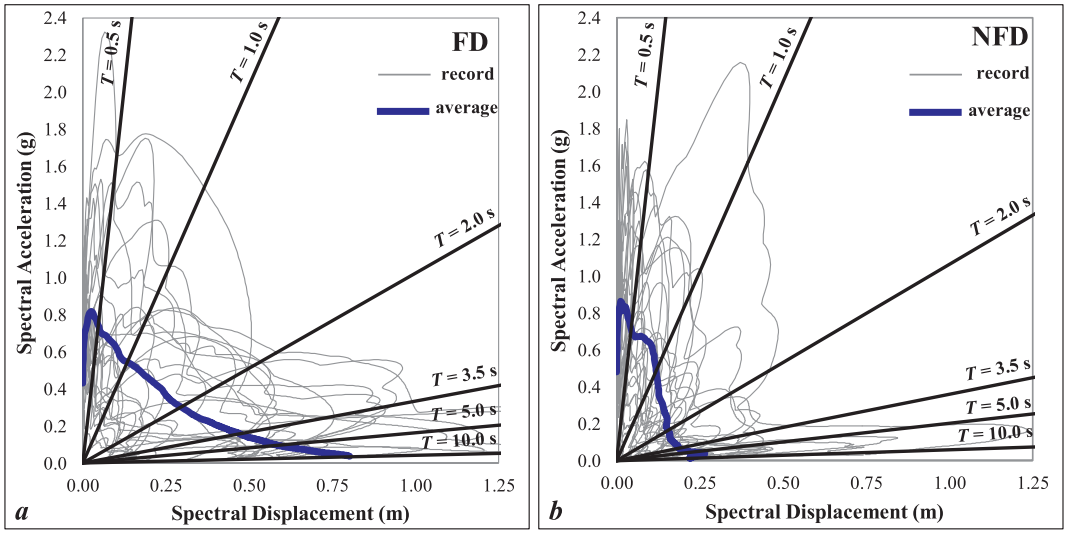


**Fig. 4.** %10 damped response spectra: (a) Forward Directivity (FD) and (b) Non-Forward Directivity (NFD).

Pacific Earthquake Engineering Research Center [58].

## 4. Time history and reliability analyses

### 4.1. Nonlinear time history analyses

In the context of the nonlinear time history analyses carried out for the reliability assessments presented in Section 4.2, base-isolated buildings described in Section 2.3 are subjected to the 54 bidirectional ground motion loadings given in Section 3 and 5000 Monte Carlo simulations are carried out for each. Thus, a total of 1.620.000 fully three-dimensional and bidirectional nonlinear time history analyses are conducted via 3D-BASIS-MONTE [32], which is a modified version of 3D-BASIS [31]. 3D-BASIS-MONTE is capable of conducting recursive nonlinear dynamic analyses of base-isolated buildings equipped with desired number of different isolation systems under the same earthquake loading by using the input data compatible with the Monte Carlo Simulation Method.

In evaluating the reliability of the buildings considering structural integrity and isolation system safety, the peak bearing displacement is taken into account as the structural response parameter. Although the inter-story drifts are better related with the integrity of the superstructure, peak bearing displacements could also be correlated with the structural integrity, indirectly, as in case the failure of the isolation system occurs due to large bearing displacements, the superstructure will be out of service and cannot be used any more. Thanks to the rigid-body behavior of the superstructure, inter-story drift ratios in base-isolated buildings typically have pretty low values [59–61] that are generally lower than the limit value of 0.01 prescribed in related seismic codes. It is suggested that this limit be kept under 0.005 for elastic superstructure behavior and protection of nonstructural elements. Since the inter-story drift ratios are calculated to be below these limits even under short period building with the largest coefficient of variation (T20COV15 case) under FD loadings [32], the reliability with respect to the maximum inter-story drift ratios is not discussed herein. Rather, the safety of both the structural integrity and the isolation system are discussed in terms of the peak bearing displacements. Due to the independent randomness of the isolator characteristic parameters, the values of these parameters are different for each isolator in each Monte Carlo Simulation cycle and thus the displacements of each isolator under the same earthquake loading differ from each other. Therefore, the highest one of the peak bearing displacements in an isolation system ($bd_{max}$) is used as the response parameter for the subject evaluation. Besides, in evaluating the safety of the vibration-sensitive contents of the buildings, the peak floor acceleration is taken into account as the structural response parameter. Since the highest accelerations are observed at the top floor, the peak accelerations at the center of mass of top floor (*tfa*) is used as the response parameter for that evaluation.

The cumulative distribution function (CDF, $F_X$) plots provide the probability of a response parameter having a value less than a specified limit value. The CDF plots of $bd_{max}$ and *tfa* are given in Figs. 5 and 6, respectively, for T20COV15 and T35COV15 isolation system subsets as representative cases. It is clearly observed from Figs. 5 and 6 that, both $bd_{max}$ and *tfa* demands obtained for FD loadings are higher than those obtained for NFD loadings. It is also seen in Fig. 5 that, $bd_{max}$ demands increase as $T_{0,nom}$ increases from 2.0 s to 3.5 s as a general trend, particularly for FD loadings. When it comes to *tfa* demands, it is observed from Fig. 6 that, *tfa* demands obtained for both FD and NFD loadings decrease as $T_{0,nom}$ increases from 2.0 s to 3.5 s. The subject CDF plots are also obtained for each of the other four building cases with the T20COV05, T20COV10, T35COV05, and T35COV10 isolation system subsets under each of the 54 earthquake loadings [32] separately, but are not presented here due to the limited space.

In order to portray the effect of the coefficient of variation on the results obtained, the CDF plots of $bd_{max}$ and *tfa* (for T20COV05, T20COV10, and T20COV15 subsets) are given in detail in Figs. 7 and 8, respectively for two representative loading cases of FD1 and FD2. As seen from these figures, *COV* values may have important effects on the reliability ($R$, see Section 4.2 for explanation of $R$) assessments depending on the specified limit value and the earthquake loading. For example, as seen in Fig. 7a, the probability of failures ($P_f$, see Section 4.2 for explanation of $P_f$) and thus the reliabilities ($R = 1 - P_f$) corresponding to the limit value of 0.80 m ($LV = 0.80$ m) are vastly different for T20COV05 ($P_f \cong 15\%$ and $R \cong 85\%$), T20COV10 ($P_f \cong 47\%$ and $R \cong 53\%$), and T20COV15 ($P_f \cong 59\%$ and $R \cong 41\%$) subsets under FD1 earthquake loading, whereas there are no differences in the probability of failures and the related reliabilities corresponding to the limit value of 0.60 m ($LV = 0.60$ m) for these subsets under the same FD1 loading (i.e., $P_f \cong 100\%$ and $R \cong 0\%$ for all). Likewise, as seen in Fig. 7b, $P_f$ and $R$ values corresponding to the limit value of 0.60 m ($LV = 0.60$ m) are considerably different for the T20COV05 ($P_f \cong 19\%$ and $R \cong 81\%$), T20COV10 ($P_f \cong 46\%$ and $R \cong 54\%$), and T20COV15 ($P_f \cong 57\%$ and $R \cong 43\%$) subsets under FD2 earthquake loading whereas there are no differences in $P_f$ and thus $R$ values corresponding to the limit value of 0.80 m ($LV = 0.80$ m) for the subject subsets under the same loading ($P_f \cong 0\%$ and $R \cong 100\%$ for all). Similar situation is observed for the peak top floor accelerations, which

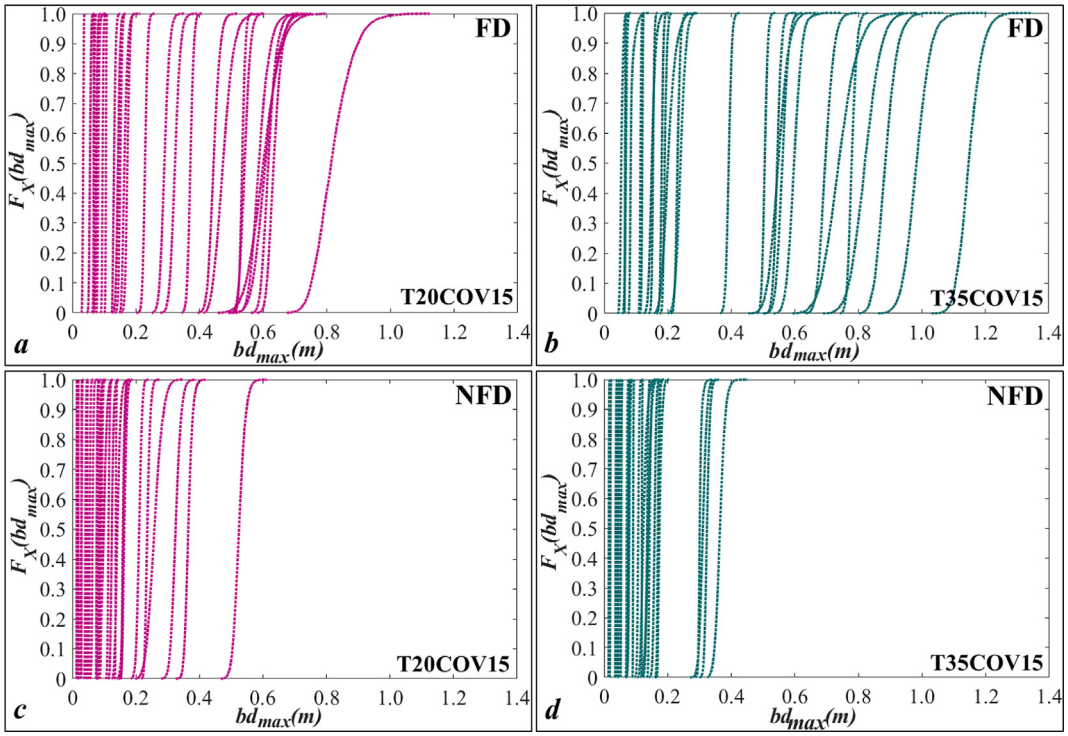


**Fig. 5.** CDF plots of the highest peak bearing displacements ($bd_{max}$) under (*a, b*) FD loadings and (*c, d*) NFD loadings. Each curve corresponds to one earthquake record given in Table 3.

can be seen in Fig. 8 clearly.

### 4.2. Reliability analyses

Seismic reliability analyses of structural systems can be conducted via many different methods using functions of limit states ($LSF(x)$), which are determined based on particular structural performance criteria such as serviceability criterion, ultimate stress or strain criterion, and etc. [18]. In structural engineering terminology, a limit state, which can be formulated as $LSF(x) = 0$, corresponds to a boundary condition between the desired and the undesired structural performance of a system [46] with respect to one of those criteria. On the

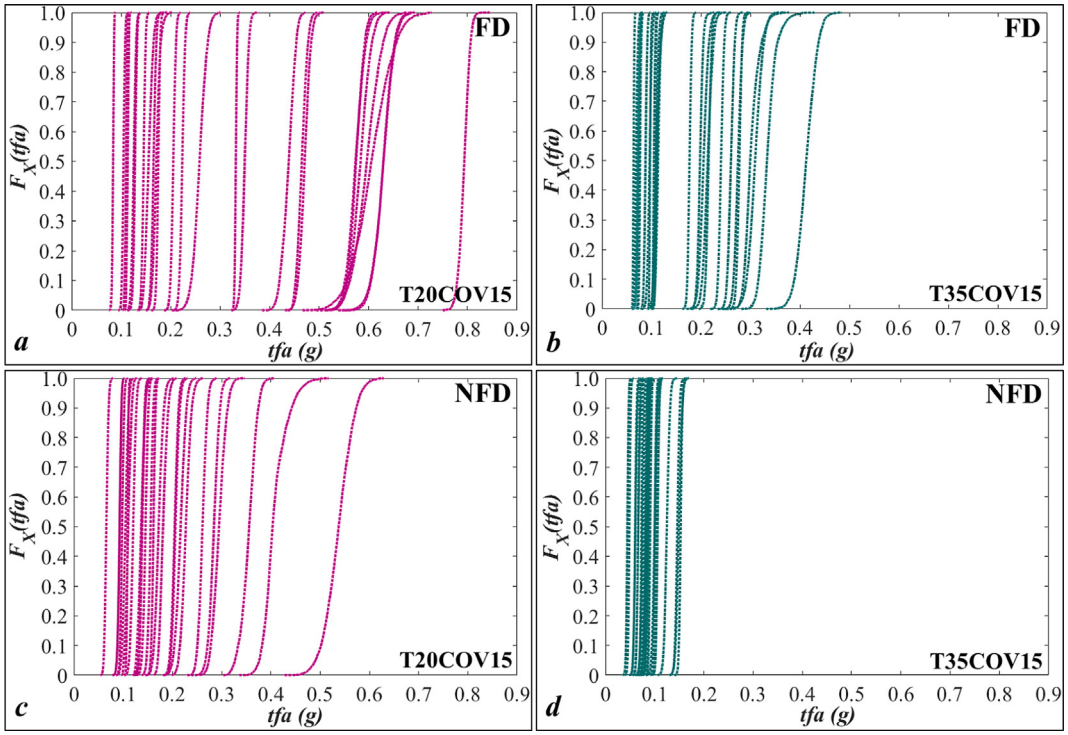


**Fig. 6.** CDF plots of the peak top floor total accelerations (*tfa*) under (*a, b*) FD loadings and (*c, d*) NFD loadings. Each curve corresponds to one earthquake record given in Table 3.

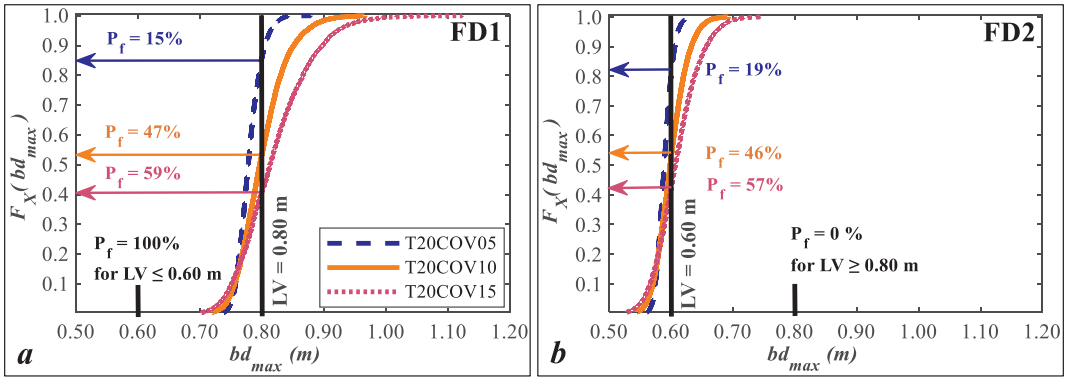


**Fig. 7.** CDF plots of the highest peak bearing displacements ($bd_{max}$) for different *COV* values under representative loadings: (*a*) FD1 and (*b*) FD2.

other hand, the failure state, which is the condition violating a limit state [18] and so corresponding to the undesired performance of the system [51], can be formulated as $LSF(x) \leq 0$. And, the reliability ($R$) of a structural system, i.e., the probability of success of that system in satisfying some performance criteria [51], is calculated by Eq. (6), where $P_f$ is the probability of failure of the limit states, i.e., the probability ($P$) of occurrence of the undesired or unsafe conditions [46] which can be determined as $P_f = P(LSF(x) \leq 0)$.

In order to calculate the probabilities of failure of a structural system considering the uncertainties, there are a number of analytical or numerical ways such as the First Order Second Moment Method, the Hasofer-Lind Method, the Second Order Reliability Method, the Monte Carlo Simulation Method, etc. [18]. The accuracy and the convenience of Monte Carlo Simulation Method (Section 2.3) in reliability analysis of complex three-dimensional and multi degree of freedom seismically isolated structural systems is demonstrated in previous studies (e.g. [19,17]). Therefore, the probabilities of failure for $bd_{max}$ and *tfa* are calculated using Eq. (7) that is developed in the context of Monte Carlo Method. In this equation, $N_{MCS}$ is the total number of Monte Carlo Simulations realized for each of the isolation system subset (which is equal to 5000 in this study) while $N_{LSF(x)\leq 0}$ is the number of failure states determined for a specific limit state function ($LSF(x)$), which is described in Eq. (8). In this equation, $response_i$ represents the value of the response parameter ($bd_{max,i}$ or $tfa_i$) obtained from the $i^{th}$ simulation while $Limit_{response}$ represents the limit state value considered for the related response parameter. In this study, 50 different displacement limit state values (See Section 4.2.1) and 40 different acceleration limit state values (See Section 4.2.2) are defined for the $bd_{max}$ and the *tfa* demands, respectively.

$$R = 1 - P_f \tag{6}$$

$$P_f = N_{LSF(x)\leq 0}/N_{MCS} \tag{7}$$

$$LSF(x) = Limit_{response} - response_i \tag{8}$$

#### 4.2.1. Reliability levels in terms of bearing displacement capacities

As reported by Pan et al. [39], the maximum design displacement values for mostly used rubber bearings (∅80 cm) in China that keeps the second place level in worldwide after Japan in terms of seismic isolation applications [14] generally vary between 45 cm and 55 cm. Likewise, the maximum design displacement capacities of HDRBs and LRBs with the same diameter used in Japan vary in the range of 40–55 cm, while the ultimate displacement capacities of those vary in the range of 55–80 cm [13]. However, manufacturers also provide higher or lower displacement capacities for rubber based bearings depending on their diameters and material properties. For example, the maximum displacement capacities of the LRBs supplied by DIS [45] are reported to change in the range of 15–91 cm. In order to cover a wide range of maximum bearing displacement demands and assess the reliabilities of the base-isolated buildings corresponding to a variety of different bearing displacement capacities, in this study 50 different displacement limit state values ($Limit_d$) are defined in the range of 2.5–125 cm with 2.5 cm increments and corresponding reliabilities are obtained via Eqs. (6)–(8) for each FD and NFD earthquake loading listed in Table 3.

The variation of the probabilities of failure ($P_f$) with respect to the closest fault distances ($r$) for each FD and NFD earthquake loading are presented in Fig. 9a and b, respectively, for a representative case, i.e. T35COV15. In Fig. 9a and b, each line of $r$ represents the result of the earthquake loading related with that fault distance value. As seen, the probabilities of failure obtained for FD loadings are significantly higher than those calculated for NFD loadings. Furthermore, the probabilities of failure obtained for FD loadings clearly increase as the closest fault distance ($r$) decreases while no such clear dependency is observed for NFD loadings. When this sensitivity of FD loadings to $r$ values are examined further, it is visually observed that the probabilities of failure

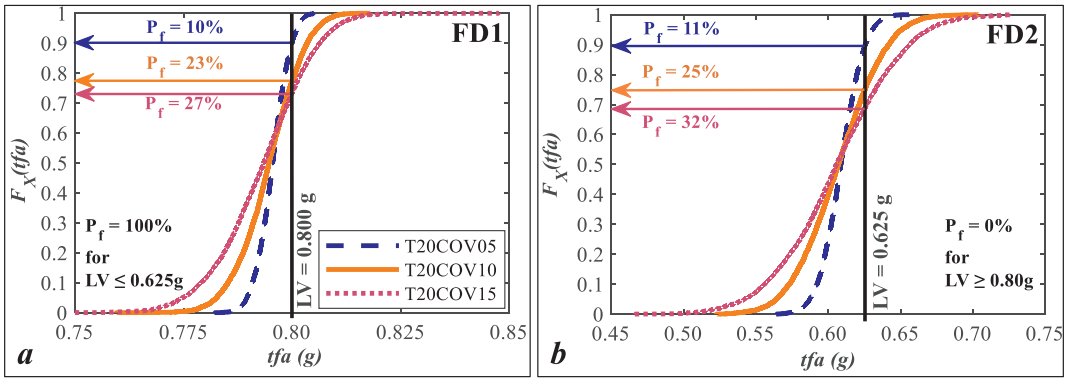


**Fig. 8.** CDF plots of the peak top floor total accelerations (*tfa*) for different *COV* values under representative loadings: (*a*) FD1 and (*b*) FD2.

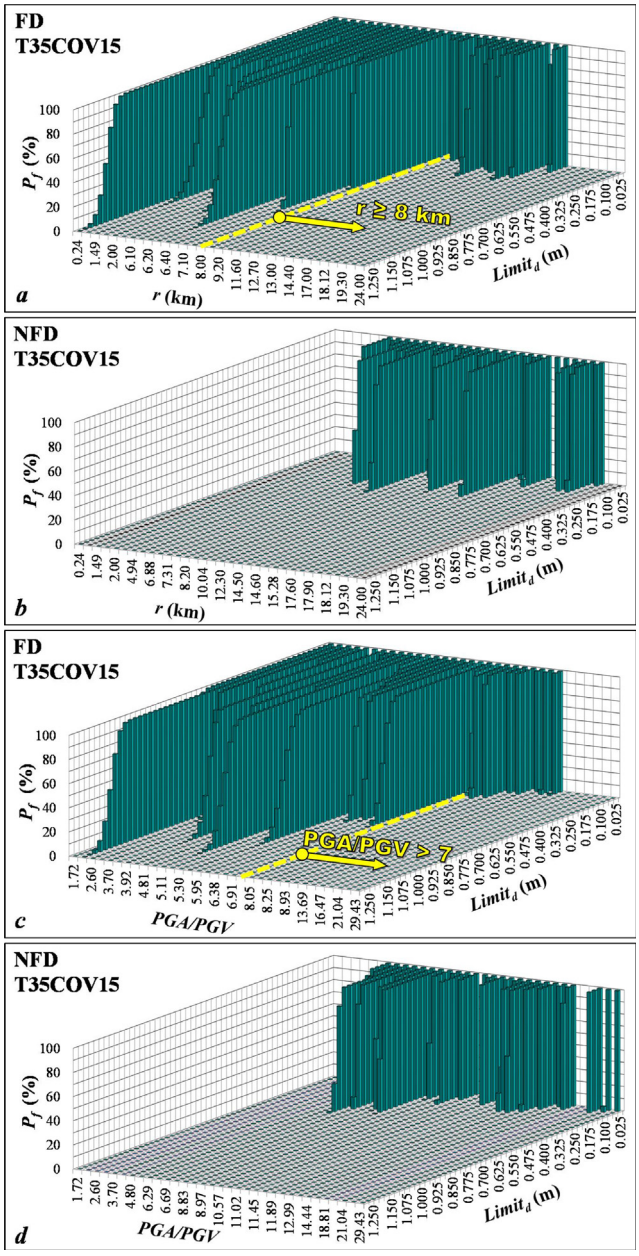


**Fig. 9.** Probabilities of failure ($P_f$) in terms of bearing displacement capacities for (*a*) FD loadings with respect to closest fault distance ($r$), (*b*) NFD loadings with respect to $r$, (*c*) FD loadings with respect to *PGA/PGV* ratio, (*d*) NFD loadings with respect to *PGA/PGV* ratio.

for FD loadings with $r < 8$ km are considerably higher than those obtained for FD loadings with $r \geq 8$ km. The probabilities of failure with respect to the *PGA/PGV* ratios under FD and NFD earthquake loadings are shown in Fig. 9c and d, respectively. In Fig. 9c and d, each line of *PGA/PGV* represents the earthquake loading related with that *PGA/PGV* ratio. The probabilities of failure obtained for FD loadings clearly increase as *PGA/PGV* ratio decreases while no such clear dependency is observed for NFD loadings. When this sensitivity of FD loadings to *PGA/PGV* ratio are examined further, it is visually observed that the probabilities of failure for FD loadings with *PGA/PGV* < 7 are considerably higher than those obtained for FD loadings with *PGA/PGV* > 7. Similar tendencies are observed for all other cases but related plots are not shown here due to the limited space.

The variation of the probabilities of failure ($P_f$) for a representative case T35COV15 are presented with respect to the pulse period ($T_p$) and the pulse amplitude ($V_p$) values of the ground motion components with forward directivity effects (FD loadings) as seen in Fig. 10a and b, respectively. In these plots, each line of $T_p$ and $V_p$ represent the earthquake loading related with that pulse period and the pulse amplitude, respectively. As a general tendency, the probabilities of failure corresponding to a selected displacement limit value ($Limit_d$) increase as $T_p$ or $V_p$ values increase. Similar tendencies are observed for all other cases but related plots are not shown here due to the limited space.

The peak bearing displacement demands in order to achieve 95% reliability level (95th percentile values) for T20COV10 and T35COV10 cases under each of FD and NFD loadings are presented in Fig. 11a and b assuming that this reliability level would be acceptable from an engineering point of view. As seen in Fig. 11a, a logarithmic trend-line is fitted that is compatible with the peak bearing displacement demand values that increase with an increasing rate as the distance to the fault decreases under FD loadings whereas no such trend is observed under NFD loadings as seen in Fig. 11b. The demands of the long-period T35COV10 case is apparently higher than the short-period T20COV10 case. Furthermore, the differences between the trend-lines for these two cases steadily increase as the fault distance decreases. In addition, there is a sudden jump in peak bearing displacement demands under FD loadings for $r < 8$ km.

The displacement demands are also evaluated with respect to three different displacement capacity levels: $Limit_{d1} = 40$ cm, $Limit_{d2} = 70$ cm, and $Limit_{d3} = 100$ cm. As seen in Fig. 11a, 95% reliability level can be achieved easily for both building cases under FD loadings with an isolator capacity of 100 cm. Note that 100 cm may be considered as the physically achievable displacement capacity level for currently used rubber bearings. This limit is exceeded for long-period T35COV10 case under one FD loading (at $r = 0.24$ km), only. 95% reliability level can also be achieved easily for both building cases in case of $r \geq 8$ km with an isolator capacity of 70 cm, which is a typical design displacement value faced in seismic prone regions (Fig. 11a). However, for $r < 8$ km, this limit is exceeded for T35COV10 case under 6 FD loadings and for T20COV10 case under 1 FD loading. When it comes to a relatively lower limit of $Limit_{d1} = 40$ cm, although 95% reliability for both building cases under FD loadings in case of $r \geq 8$ km is achieved, both building cases under FD loadings for $r < 8$ km is challenged by this limit (Fig. 11a). On the other hand, it is seen that 95% reliability level is easily achieved by both building cases under NFD loadings even for $Limit_{d1} = 40$ cm (Fig. 11b).

Average of all probabilities of failure ($P_f$) and thus all average reliabilities ($R$) for each case (T20COV05, T20COV10, T20COV15, T35COV05, T35COV10, and T35COV15) corresponding to each limit state value are calculated for the group of FD and NFD earthquake loadings and further discussions are made using the plots representing these average reliabilities (Fig. 12). It is seen from Fig. 12 that the average reliabilities obtained for NFD loadings are remarkably higher than those calculated for FD loadings. Secondly, the average reliabilities based on the bearing displacement demands decrease as $T_{0,nom}$ increases from 2.0 s to 3.5 s particularly for FD loadings. As the third observation, it is seen that the average reliability values show little sensitivity to *COV* values for both FD and NFD loadings. When *COV* increases from 5% to 15%, the changes in average reliabilities are calculated to be up to 5.27% and 2.48% for FD and NFD loadings, respectively.

As discussed and exemplified using case T35COV15 earlier (see Fig. 9), the $P_f$, thus the reliabilities for FD loadings are sensitive to the closest fault distance ($r$) and *PGA/PGV* ratio. This phenomenon is further examined here in terms of average reliabilities. The average reliabilities for FD loadings with $r < 8$ km and $r \geq 8$ km are given in Fig. 13a and b, respectively while those with *PGA/PGV* < 7 and *PGA/PGV* > 7 are given in Fig. 14a and b, respectively. It is observed that the average reliabilities for FD loadings with $r < 8$ km are considerably lower than those with $r \geq 8$ km, and the average reliabilities for FD loadings with *PGA/PGV* < 7 are considerably lower than those with

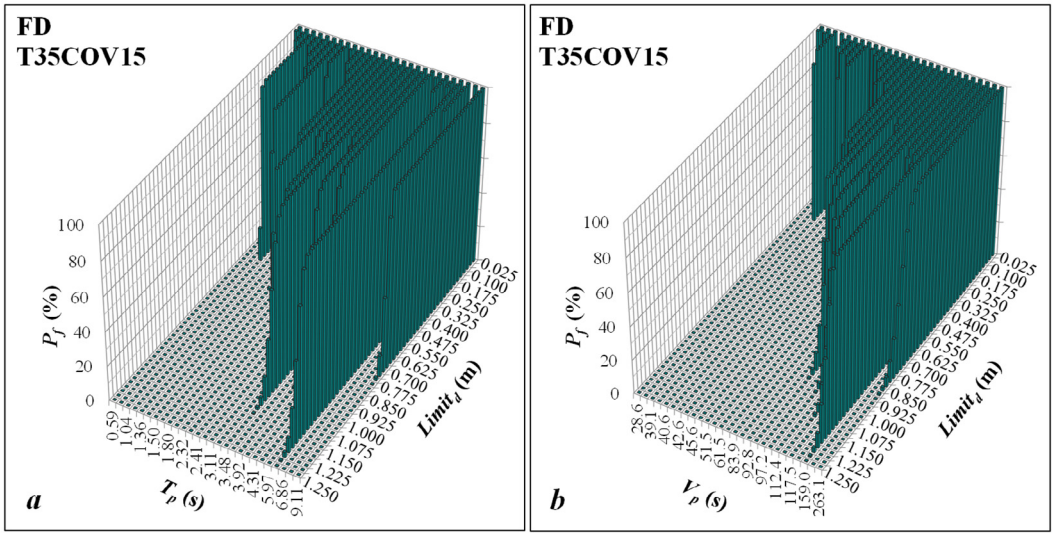


**Fig. 10.** Probabilities of failure ($P_f$) in terms of bearing displacement capacities for FD loadings (a) with respect to pulse period ($T_p$), (b) with respect to pulse amplitude ($V_p$).

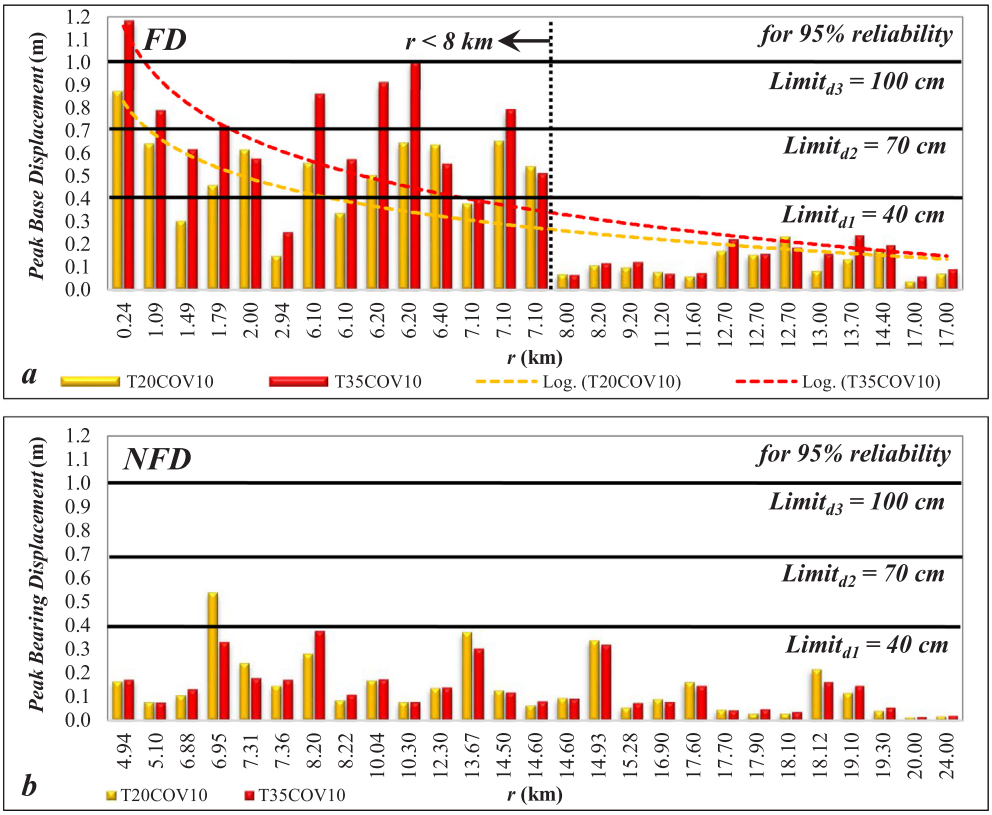


**Fig. 11.** Peak bearing displacement demands for 95% reliability level for T20COV10 and T35COV10 under: (a) FD loadings, (b) NFD loadings.

*PGA/PGV* > 7. In addition, the average reliabilities for NFD loadings (Fig. 12b) are close to the ones for the FD loadings with $r \geq 8$ km and *PGA/PGV* > 7. For example, under FD loadings with $r \geq 8$ km and/or *PGA/PGV* > 7, all buildings with $T_{0,nom} = 2.0$ s and $T_{0,nom} = 3.5$ s are reliable ($R = 99.98\%$) considering $Limit_d = 30$ cm (Figs. 13b and 14b) while under NFD loadings, about 88% of those are reliable with respect to the same displacement limit value (Fig. 12b). However, under FD loadings with $r < 8$ km, only about 13% and 7% of the buildings with $T_{0,nom} = 2.0$ s and $T_{0,nom} = 3.5$ s, respectively, seem to be reliable with respect to the same displacement limit value (Fig. 13a). Considering the same limit value, the average reliabilities are calculated as about 36% and 32% for $T_{0,nom} = 2.0$ s and 3.5 s buildings, respectively, under FD loadings with *PGA/PGV* < 7 (Fig. 14a).

It should also be noted here that, the plots given in Figs. 12–14 provide a comprehensive picture in terms of the reliability level of the structural system for any selected bearing displacement capacity or can be used to determine the bearing displacement capacities that should be selected in order to achieve a specified reliability level. For example, if the target reliability level is assumed as $R = 95\%$, the bearing displacement capacities should selected at least about 80 cm and 115 cm for buildings with $T_{0,nom} = 2.0$ s and $T_{0,nom} = 3.5$ s in case of FD loadings with $r < 8$ km and *PGA/PGV* < 7 as seen in Figs. 13a and 14a,

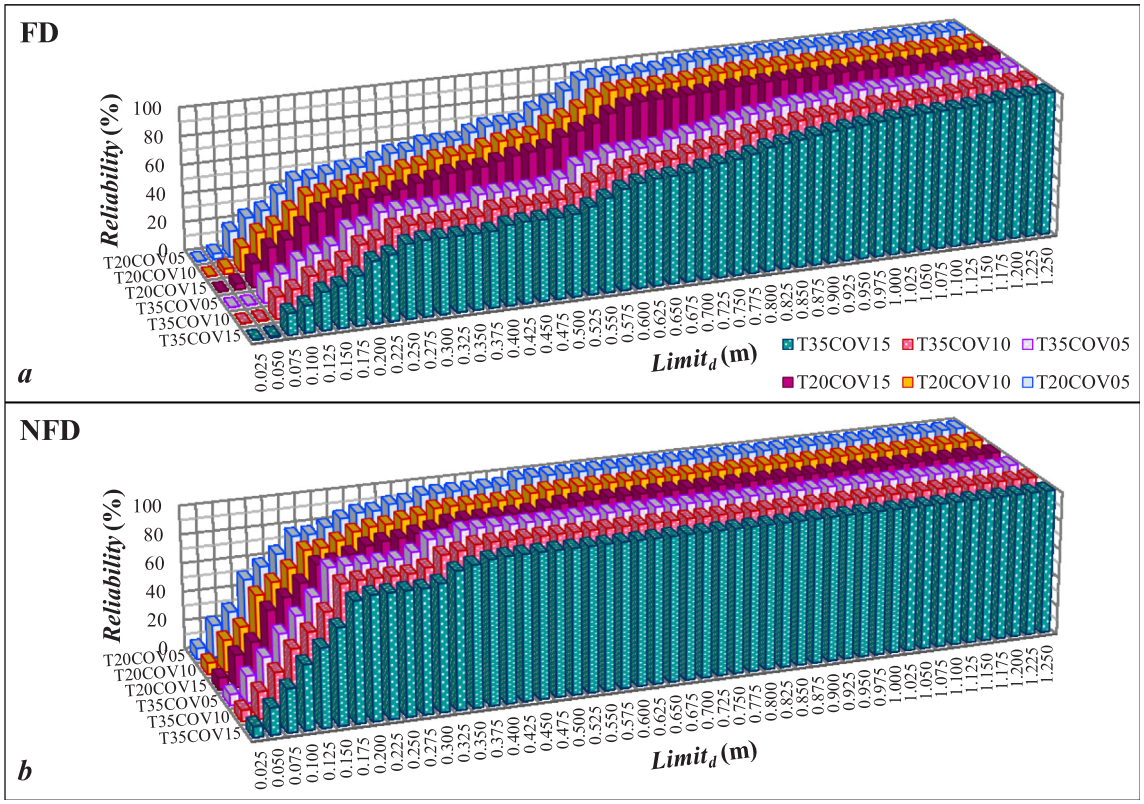


**Fig. 12.** Average reliabilities for $bd_{max}$ demands under (*a*) FD and (*b*) NFD loadings.

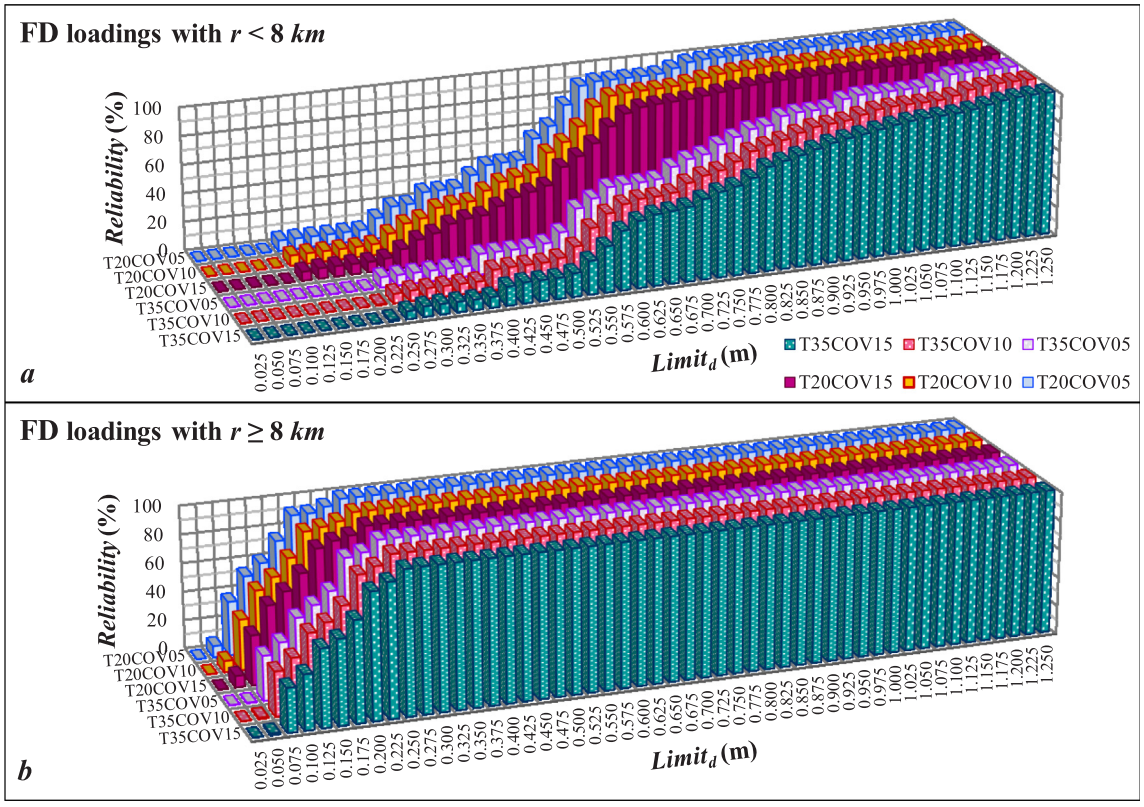


**Fig. 13.** Average reliabilities for $bd_{max}$ demands under FD loadings (*a*) $r < 8$ km and (*b*) $r \geq 8$ km.

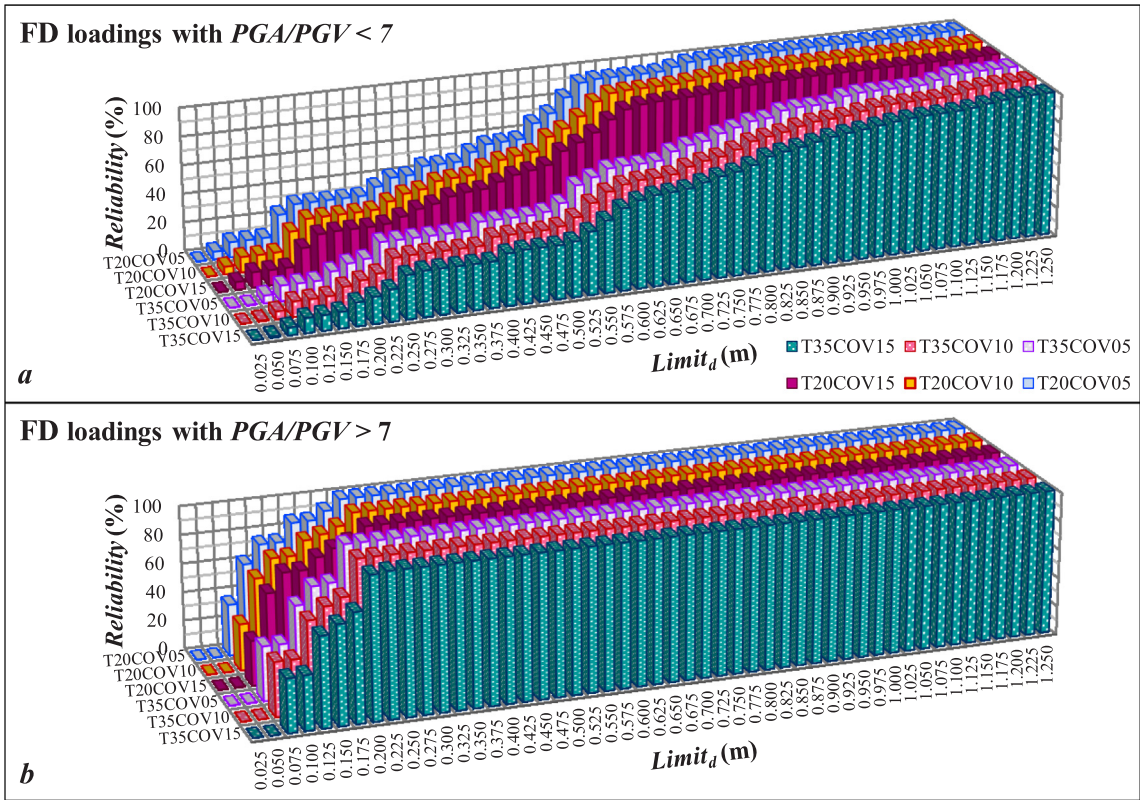


**Fig. 14.** Average reliabilities for $bd_{max}$ demands under FD loadings (*a*) *PGA/PGV* < 7 and (*b*) *PGA/PGV* > 7.

respectively. On the other hand, under FD loadings with $r \geq 8$ km and *PGA/PGV* > 7 (Figs. 13b and 14b, respectively), the bearing displacement capacity value can be selected at least about 25 cm for all building cases in order to achieve the same reliability level ($R$ = 95%). Likewise, in order to achieve at least 95% reliability, the corresponding bearing displacement capacity should be selected at least about 37.5 cm for all the benchmark building cases under NFD loadings as seen in Fig. 12b.

#### 4.2.2. Reliability levels in terms of floor accelerations

The peak floor acceleration is among the most important structural response parameters for base-isolated buildings since it controls the safety and serviceability of the contents of those buildings [2]. Therefore, in order to avoid from high floor accelerations that may damage building contents, the subject response parameter is typically taken into consideration in the design phase of those buildings. But, there is no explicitly determined limit for the peak floor accelerations in seismic design codes [13]. On the other hand, based on some experimental studies carried out by Mizuno et al. [62], horizontal peak floor accelerations should be limited to 3.0 m/s$^2$ (≈0.30 g) for medical, electronical and other important facilities. Moreover, in order to avoid from permanent damage and loss of data for some disc drives in either operating or non-operating conditions, the peak horizontal floor accelerations should not exceed the limit values varying in the range of 0.2–1.0 g according to Worksafe Technologies [63]. Additionally, the statistics conducted for base-isolation design by Architectural Institute of Japan [64] and a study by Alhan and Şahin [65] showed that the highest peak floor accelerations generally occur at the top floors of the base-isolated buildings. In this study, in order to assess the reliabilities of the base-isolated buildings and their vibration sensitive contents in terms of floor accelerations, peak top floor acceleration (*tfa*) demands are compared to 40 different acceleration limit state values ($Limit_a$) which are defined in the range of 0.025–1.00 g with 0.025 g increments. And, *tfa* demands obtained for a building case under an earthquake loading are compared with those 40 limit state values using Eq. (8) in order to calculate the probabilities of failure ($P_f$, Eq. (7)) and thus the reliabilities ($R$, Eq. (6)) for the subject building case under the subject earthquake loading. This process is repeated for all the building cases under each ground motion loading given in Table 3.

The variation of the probabilities of failure ($P_f$) corresponding to the acceleration limit values ($Limit_a$) for each FD and NFD earthquake loading are presented with respect to the closest fault distances ($r$) in Fig. 15a and b, respectively, for a representative case, i.e. T20COV15. In these plots, each line of $r$ represents the result of the earthquake loading related with that fault distance value. The probabilities of failure calculated for *tfa* demands obtained under FD loadings are significantly higher than those calculated for NFD loadings. Furthermore, the probabilities of failure calculated for *tfa* demands obtained under FD loadings also clearly increase as the closest fault distance ($r$) decreases while no such clear dependency is observed for NFD loadings. It is visually observed that the probabilities of failure calculated for *tfa* demands obtained under FD loadings with $r$ < 8 km are considerably higher than those obtained for FD loadings with $r \geq 8$ km (Fig. 15a). The probabilities of failure with respect to the *PGA/PGV* ratios under FD and NFD earthquake loadings are shown in Fig. 15c and d, respectively. Here, each line of *PGA/PGV* represents the earthquake loading related with that *PGA/PGV* ratio. The probabilities of failure calculated for *tfa* demands obtained under FD loadings also clearly increase as *PGA/PGV* ratio decreases while no such clear dependency is observed for NFD loadings. It is visually observed that the probabilities of failure for FD loadings with *PGA/PGV* < 7 are considerably higher than those obtained for FD loadings with *PGA/PGV* > 7 (Fig. 15c). Similar tendencies are observed for all other cases but related plots are not shown here due to the limited space.

The variation of the probabilities of failure ($P_f$) for a representative case T20COV15 are presented with respect to the pulse period ($T_p$) and the pulse amplitude ($V_p$) values of the ground motion components with forward directivity effects (FD loadings) as seen in Fig. 16a and b,

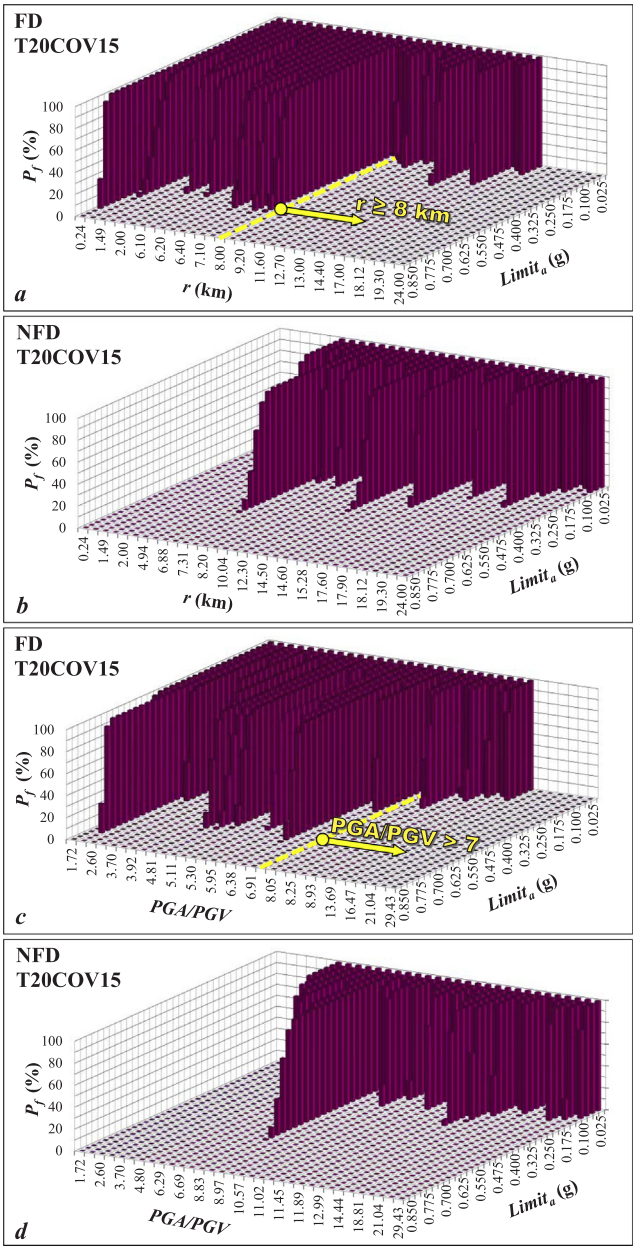


**Fig. 15.** Probabilities of failure ($P_f$) in terms of floor accelerations for (*a*) FD loadings with respect to *r*, (*b*) NFD loadings with respect to *r*, (*c*) FD loadings with respect to *PGA/PGV* ratio, (*d*) NFD loadings with respect to *PGA/PGV* ratio.

respectively. In these plots, each line of $T_p$ and $V_p$ represent the earthquake loading related with that pulse period and the pulse amplitude, respectively. As a general tendency, the probabilities of failure corresponding to a selected acceleration limit value ($Limit_a$) increase as $T_p$ or $V_p$ values increase. Similar tendencies are observed for all other cases but related plots are not shown here due to the limited space.

The peak top floor accelerations of T20COV10 and T35COV10 cases under FD and NFD loadings are also evaluated with respect to the 95% reliability level assuming that this reliability level would be acceptable from an engineering point of view. The peak top floor acceleration demands in order to achieve 95% reliability level (95th percentile values) for T20COV10 and T35COV10 cases under each of FD and NFD loadings are presented in Fig. 17a and b. Similar to the peak bearing displacement demands, a logarithmic trend-line is fitted that is compatible with the peak top floor acceleration demands that increase with an increasing rate as the distance to the fault decreases under FD loadings as seen in Fig. 17a, whereas no such trend is observed under NFD loadings as seen in Fig. 17b. The peak top floor acceleration demands of the short-period T20COV10 case is apparently higher than the long-period T35COV10 case contrary to the peak bearing displacement demands. Furthermore, the differences between the trend-lines for these two cases steadily increase as the fault distance decreases. In addition, there is also a sudden jump in peak top floor acceleration demands under FD loadings for $r < 8$ km.

The acceleration demands are also evaluated with respect to three different acceleration limit levels which may be considered as important limit levels for protection of the building and/or safety of the vibration sensitive contents of the buildings: $Limit_{a1} = 0.2$ g, $Limit_{a2} = 0.5$ g, $Limit_{a3} = 1.0$ g. As seen in Fig. 17a, 95% reliability level can be achieved easily in case of $Limit_{a3} = 1.0$ g, which may be considered as a high limit representing the protection of building itself from extensive damage. In this case, the peak floor acceleration demands for 95% reliability level do not exceed the limit of 1.0 g for both buildings under all FD loadings. In addition, 95% reliability level can also be achieved for protecting the vibration sensitive contents (which can resist to 0.5 g at maximum – typically in non-operating conditions) of both building cases under FD loadings for $r \geq 8$ km. For $r < 8$ km, this limit is exceeded for T20COV10 case under many of FD loadings, while it is not exceeded for T35COV10. When it comes to the lowest acceleration limit value, i.e., $Limit_{a1} = 0.2$ g, although 95% reliability for protecting the vibration sensitive contents (which may resist to 0.2 g at maximum – typically in operating conditions) of both building cases under FD loadings in case of $r \geq 8$ km is achieved, a challenge is faced for $r < 8$ km (Fig. 17a) as this limit can't be met for most FD loadings even by long-period T35COV10 isolation system. On the other hand, as seen in Fig. 17b, 95% reliability is achieved by T35COV10 case under NFD loadings even for $Limit_{a1} = 0.2$ g. However, sensitive contents of T20COV10 building case under NFD loadings are challenged by $Limit_{a1} = 0.2$ g, while other limits (i.e. 0.5 g and 1.0 g) are met except for one NFD loading case ($r = 6.95$ km) which exceeds $Limit_{a2} = 0.5$ g.

Average of all probabilities of failure ($P_f$) and thus all average reliabilities ($R$) for each case (T20COV05, T20COV10, T20COV15, T35COV05, T35COV10, and T35COV15) corresponding to each acceleration limit state value are calculated for the group of FD and NFD earthquake loadings and further discussions are made using the plots representing these average reliabilities (Fig. 18). It is seen from Fig. 18 that, the average reliabilities calculated for *tfa* demands obtained under NFD loadings are higher than those calculated for FD loadings. Secondly, the average reliabilities based on the peak top floor acceleration demands increase as $T_{0,nom}$ increases from 2.0 s to 3.5 s particularly for FD loadings. As the third observation, it is seen that the average reliability values calculated for *tfa* demands show little sensitivity to *COV* values. When *COV* increases from 5% to 15%, the changes in average reliabilities are calculated to be up to 3.02% and 2.68% for FD and NFD loadings, respectively.

As discussed and exemplified using case T35COV15 earlier (see Fig. 15), the probabilities of failure and thus the reliabilities for FD loadings are sensitive to the closest fault distance ($r$) and *PGA/PGV* ratio. This phenomenon is further examined here in terms of average reliabilities. It is observed that the average reliabilities for FD loadings with $r < 8$ km are considerably lower than those obtained for FD loadings with $r \geq 8$ km (Fig. 19) and the average reliabilities for FD loadings with $PGA/PGV < 7$ are considerably lower than those obtained for FD loadings with $PGA/PGV > 7$ (Fig. 20). In addition, the average reliabilities calculated based on *tfa* demands under NFD loadings (Fig. 18b) are close to the ones for the FD loadings with $r \geq 8$ km (Fig. 19b) and with $PGA/PGV > 7$ (Fig. 20b). For example, under FD loadings with $r \geq 8$ km and/or $PGA/PGV > 7$, all of the buildings ($R = 99.98\%$) with $T_{0,nom} = 2.0$ s and $T_{0,nom} = 3.5$ s are reliable considering $Limit_a = 0.3$ g (Figs. 19b and 20b) while under NFD loadings all of the buildings ($R = 99.98\%$) with $T_{0,nom} = 2.0$ s and about 88% of

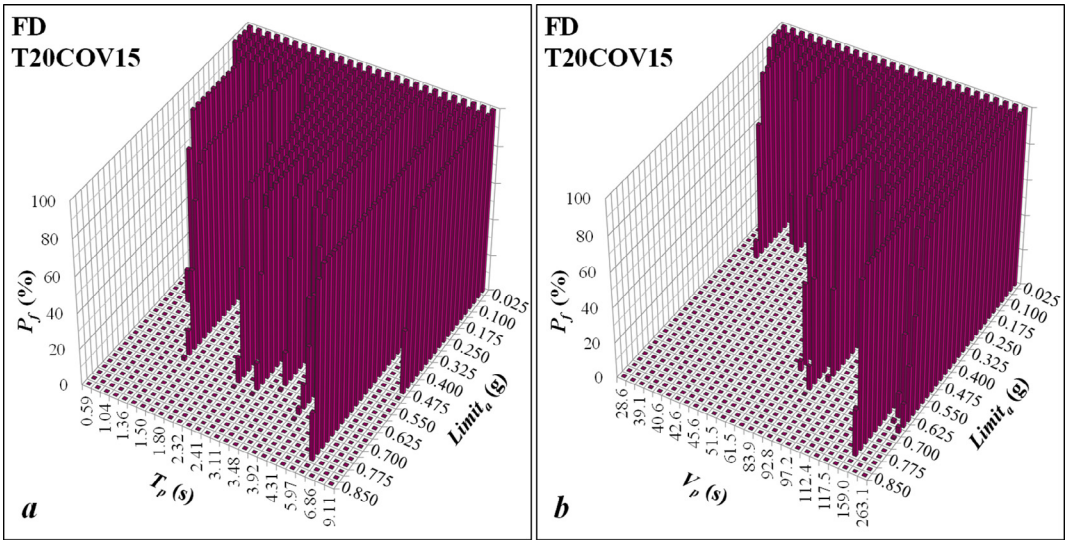


**Fig. 16.** Probabilities of failure ($P_f$) in terms of peak top floor accelerations for FD loadings (*a*) with respect to pulse period ($T_p$), (*b*) with respect to pulse amplitude ($V_p$).

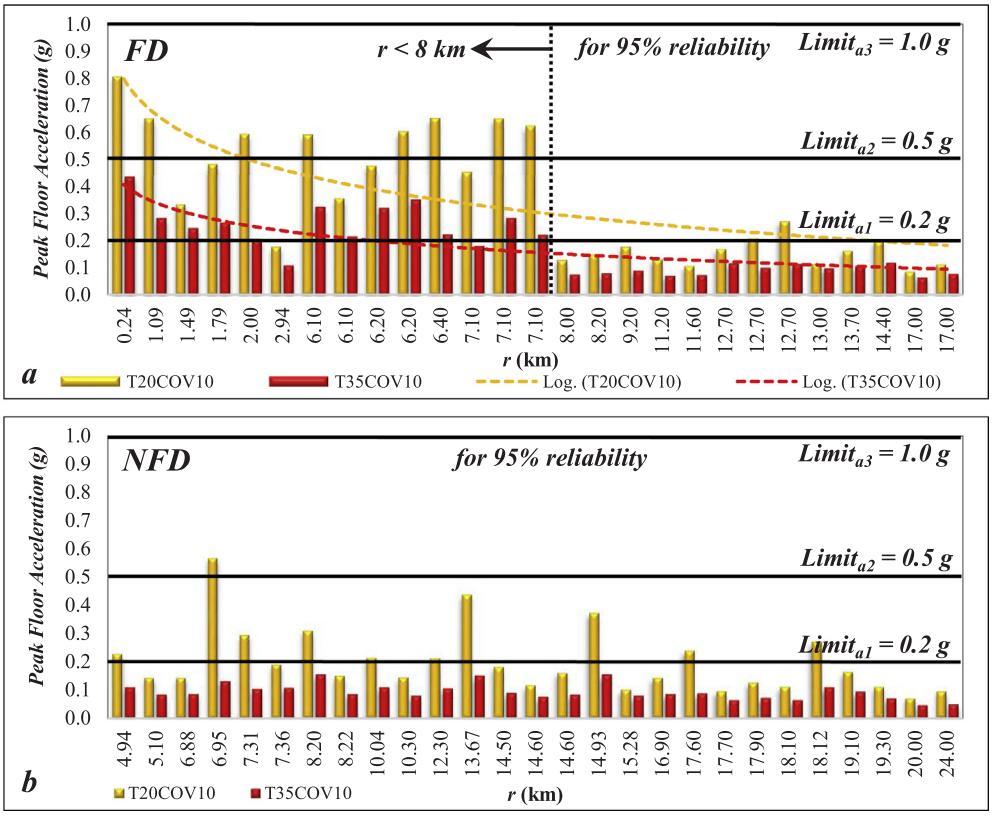


**Fig. 17.** Peak floor acceleration demands for 95% reliability level for T20COV10 and T35COV10 under: (a) FD loadings, (b) NFD loadings.

the buildings ($R \cong 88\%$) with $T_{0,nom} = 3.5$ s seem to be reliable with respect to the same acceleration limit (Fig. 18b). However, under FD loadings with $r < 8$ km, only about 7% and 75% of the buildings with $T_{0,nom} = 2.0$ s and $T_{0,nom} = 3.5$ s, respectively, seem to be reliable with respect to $Limit_a = 0.3$ g (Fig. 19a). Considering the same limit value, the average reliabilities are calculated as about 32% and 82% for $T_{0,nom} = 2.0$ s and $T_{0,nom} = 3.5$ s buildings, respectively, under FD loadings with $PGA/PGV < 7$ (Fig. 20a).

It should also be noted that, the plots given in Figs. 18–20 provide a comprehensive picture in terms of the reliability level of the building itself and/or the vibration sensitive contents of the structural system for any selected floor acceleration value, or can be used to determine the floor acceleration value that should not be exceeded in order to achieve a specified reliability level. For example, the target reliability level of $R = 95\%$ can be achieved only if $Limit_a \geq 0.800$ g for $T_{0,nom} = 2.0$ s buildings and $Limit_a \geq 0.425$ g for $T_{0,nom} = 3.5$ s buildings in case of FD loadings with $r < 8$ km and $PGA/PGV < 7$ (Figs. 19a and 20a, respectively). On the other hand, under FD loadings with $r \geq 8$ km and $PGA/PGV > 7$, the same reliability level ($R = 95\%$) can be achieved for even $Limit_a \geq 0.275$ g and $Limit_a \geq 0.125$ g for $T_{0,nom} = 2.0$ s and $T_{0,nom} = 3.5$ s buildings, respectively (Figs. 19b and 20b, respectively). Likewise, under NFD loadings (Fig. 18b), 95% reliability can be

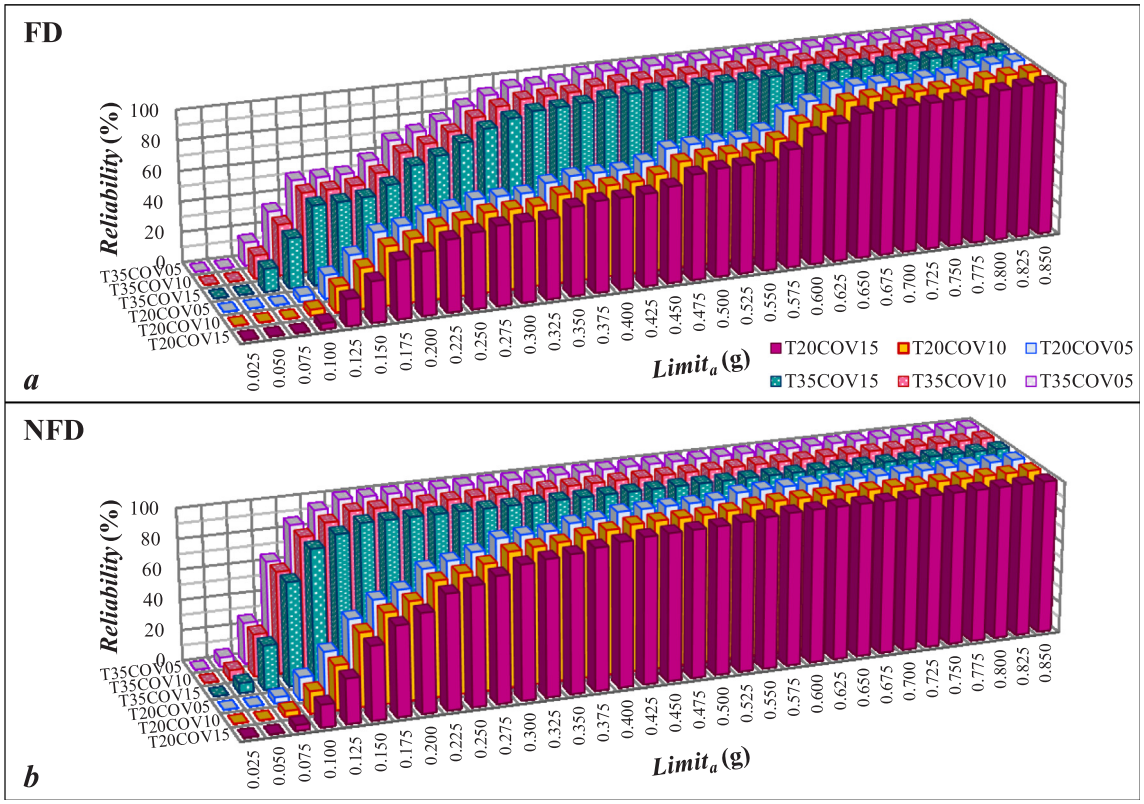


**Fig. 18.** Average reliabilities for *tfa* demands under (*a*) FD and (*b*) NFD loadings.

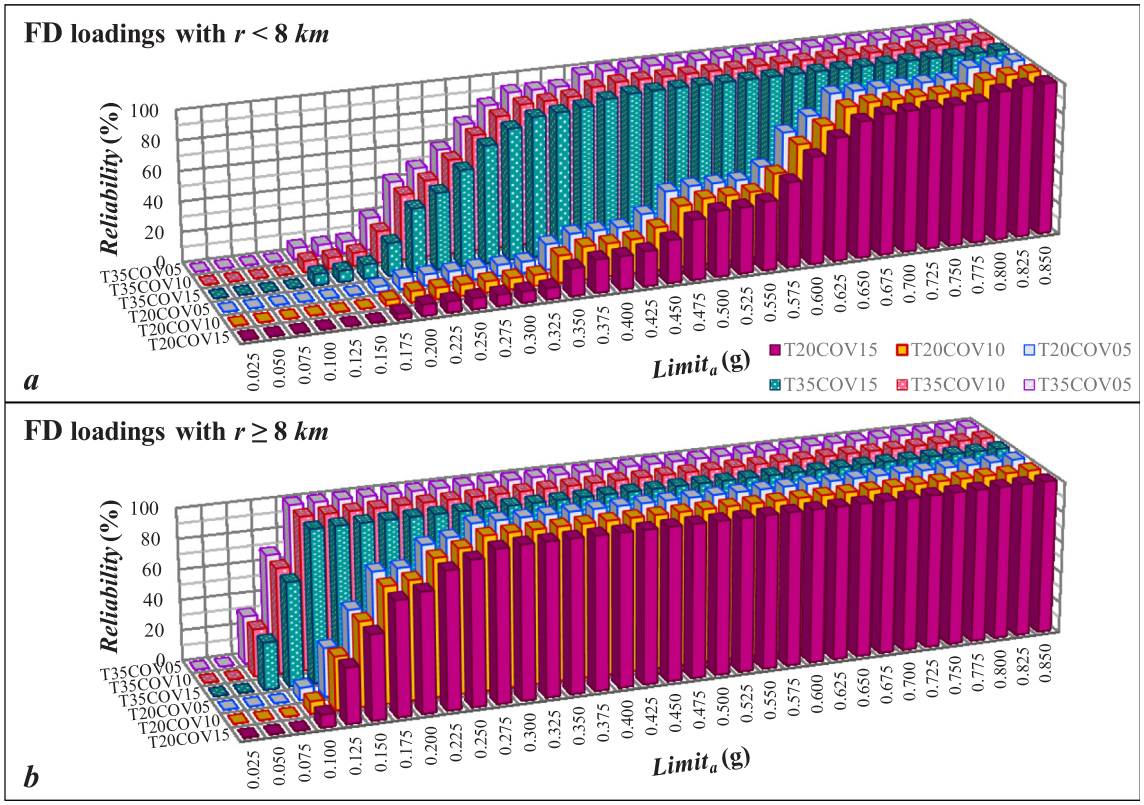


**Fig. 19.** Average reliabilities for tfa demands under FD loadings (a) $r < 8$ km and (b) $r \geq 8$ km.

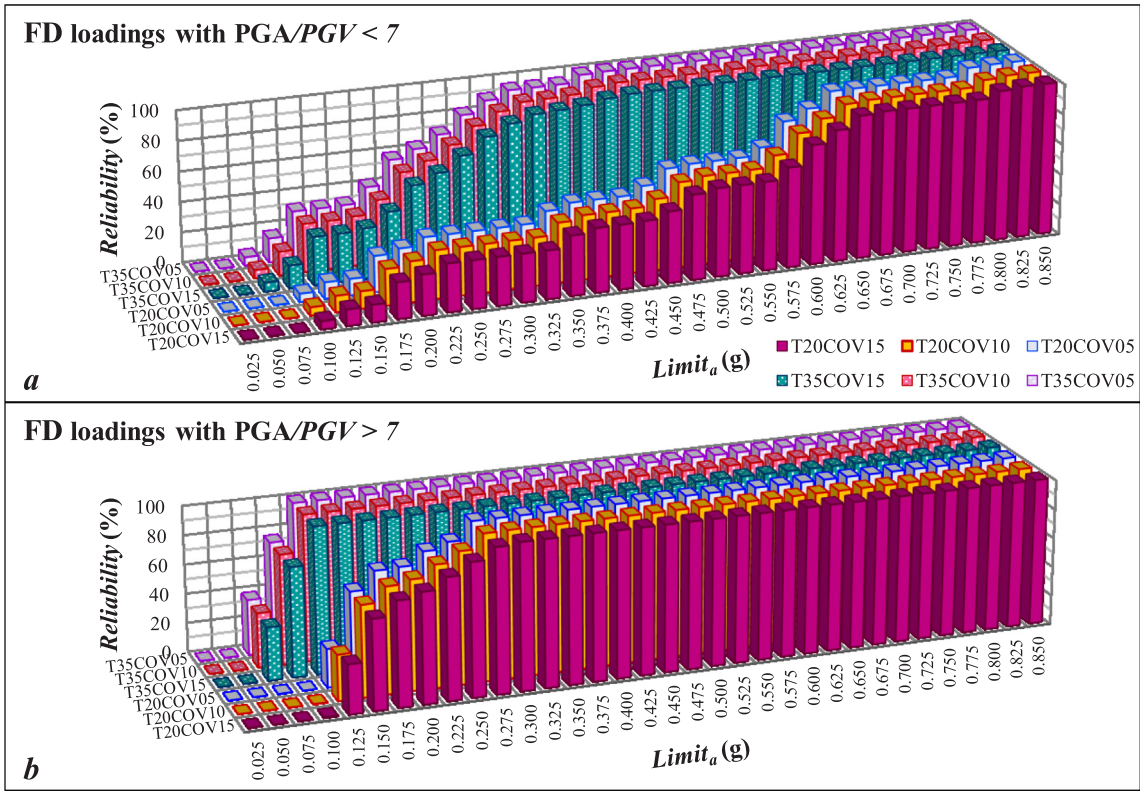


**Fig. 20.** Average reliabilities for *tfa* demands under FD loadings (a) $PGA/PGV < 7$ and (b) $PGA/PGV > 7$.

achieved for $Limit_a \geq 0.425$ g and for even $Limit_a \geq 0.175$ g for $T_{0,nom} = 2.0$ s and $T_{0,nom} = 3.5$ s buildings, respectively.

## 5. Conclusions

In this study, seismic reliability of buildings with elastomeric base-isolation systems is investigated using realistic fully three-dimensional benchmark buildings considering the uncertainties in the isolation system characteristics and the inherent record-to-record variabilities in the ground motion records. Large sets of historical near-fault ground motions with forward-directivity effects (FD) or without forward-directivity effects (NFD) are used. Two different levels of nominal isolation periods ($T_{0,nom} = 2.0$ s and $T_{0,nom} = 3.5$ s) and three different levels of uncertainty (Coefficient Of Variation; $COV = 5\%$, 10%, 15%) are taken into account. The reliability of the buildings is investigated in terms of structural integrity, isolation system safety, and the safety of the vibration-sensitive contents of the buildings using the highest peak bearing displacements and the peak top floor accelerations obtained from the nonlinear time history analyses conducted in the framework of the Monte Carlo simulations. The conclusions are summarized below:

1- The reliability plots presented here provide a comprehensive picture in terms of the reliability level of a typical base-isolated building and its vibration sensitive contents. They can be used to determine the bearing displacement or the floor acceleration limit values that should not be exceeded in order to achieve a specified reliability level.
2- It is revealed that the record-to-record variability has the most important effect. That is, seismic reliabilities of base-isolated buildings are much more dependent on the characteristics of ground motions than the uncertainties in the mechanical characteristics of the isolation systems.
3- Seismic reliabilities for FD loadings are sensitive to the closest fault distance ($r$), $PGA/PGV$ ratios, pulse periods, and pulse amplitudes of ground motions. As a general trend, as $r$ and $PGA/PGV$ decrease and pulse periods and pulse amplitudes increase, they decrease for both bearing displacements and floor accelerations. However, no such clear dependency is observed under NFD loadings.
4- The average reliabilities for both bearing displacements and floor accelerations under FD loadings with $r < 8$ km and $PGA/PGV < 7$ are considerably lower than those obtained for FD loadings with $r \geq 8$ km and $PGA/PGV > 7$, respectively.
5- The average reliabilities are sensitive to the nominal isolation periods. The average reliabilities calculated based on the peak bearing displacements decrease as nominal isolation period increases from 2.0 s to 3.5 s, particularly for FD loadings, whereas the average reliabilities calculated based on the peak top floor accelerations increase as nominal isolation period increases from 2.0 s to 3.5 s.
6- The level of uncertainty, represented by $COV$, may have important effects on the probability of failure values for a specific limit value under a specific earthquake loading. However, on average, the probability of failure values calculated for both peak bearing displacement and peak top floor acceleration demands obtained under FD and NFD loadings show little sensitivity to $COV$ values.

## Acknowledgments

This work was supported by Scientific Research Projects Coordination Unit of Istanbul University, Turkey. Project number: 20206.

## References

[1] Cardone D, Perrone G, Piesco V. Developing collapse fragility curves for base-isolated buildings. Earthquake Engng Struct Dyn 2019;48:78–102.
[2] Alhan C, Hısman K. Seismic isolation performance sensitivity to potential deviations from design values. Smart Struct Syst 2016;18:293–315.
[3] Sanchez J, Masroor A, Mosqueda G, Ryan K. Static and dynamic stability of elastomeric bearings for seismic protection of structures. J Struct Eng 2013;139:1149–59.

[4] Montuori GM, Mele E, Marrazzo G, Brandonisio G, De Luca A. Stability issues and pressure-shear interaction in elastomeric bearings: the primary role of the secondary shape factor. Bull Earthq Eng 2016;14(2):569–97.
[5] Cardone D, Perrone G. Critical load of slender elastomeric seismic isolators: an experimental perspective. Eng Struct 2012;40:198–204.
[6] Dorfmann A, Burtscher SL. Aspects of cavitation damage in seismic bearings. J Struct Eng 2000:573–9.
[7] Kumar M, Whittaker A, Constantinou M. Experimental investigation of cavitation in elastomeric seismic isolation bearings. Eng Struct 2015;101:290–305.
[8] Muramatsu Y, Inoue K, Katoh R, Kamitani N, Sakahuchi T, Sasaki Y, et al. Test results of ultimate properties of rubber bearings for buildings. AIJ J Technol Des 2004;10(20):67–70.
[9] Cheng FY, Jiang H, Lou K. Smart structures innovative systems for seismic response control. Boca Raton: CRC Press Taylor and Francis Group; 2008.
[10] Constantinou MC, Whittaker AS, Kalpakidis Y, Fenz DM, Warn GP. Performance of seismic isolation hardware under service and seismic loading, Technical Report MCEER-07-0012. Buffalo: The State University of New York; 2007.
[11] Kalpakidis IV, Constantinou MC, Whittaker AS. Effects of large cumulative travel on the behavior of lead-rubber seismic ısolation bearings. J Struct Eng 2010;136(5):491–501.
[12] Cardone D, Gesualdi G. Experimental evaluation of the mechanical behavior of elastomeric materials for seismic applications at different air temperatures. Int J Mech Sci 2012;64:127–43.
[13] Pan P, Zamfirescu D, Nakashima M, Nakayasu N, Kashiwa H. Base isolation design practice in Japan: introduction to the post-Kobe approach. J Earthquake Eng 2005;9:147–71.
[14] Martelli A, Clemente P, De Stefano A, Forni M, Salvatori A. Recent development and application of seismic isolation and energy dissipation and conditions for their correct use. In: Ansal A, editor. Perspectives on European earthquake engineering and seismology. Geotechnical, geological and earthquake engineering. Cham: Springer; 2014.
[15] De La Llera JC, Inaudi JA. Analysis of base-isolated buildings considering stiffness uncertainty in the isolation system. Fifth national conference on earthquake engineering, Illionis Chicago. 1994. p. 623–32.
[16] ShentonIII HW, Holloway ES. Effect of stiffness variability on the response of isolated structures. Earthquake Eng Struct Dyn 2000;29:19–36.
[17] Alhan C, Gavin HP. Reliability of base isolation for the protection of critical equipment from earthquake hazards. Eng Struct 2005;27:1435–49.
[18] Datta TK. Seismic analysis of structures. Singapore: John Wiley and Sons (Asia) Pte Ltd.; 2010. ISBN: 978-0-470-82461-0.
[19] Pradlwarter HJ, Schuëller GI, Dorka U. Reliability of MDOF-systems with hysteretic devices. Eng Struct 1998;20(8):685–91.
[20] Chen J, Liu W, Peng Y, Li J. Stochastic seismic response and reliability analysis of base-isolated structures. J Earthquake Eng 2007;11:903–24.
[21] Morgan TA, Mahin SA. Achieving reliable seismic performance enhancement using multi-stage friction pendulum isolators. Earthquake Engng Struct Dyn 2010;39:1443–61.
[22] Taflanidis AA, Jia G. A simulation-based framework for risk assessment and probabilistic sensitivity analysis of base-isolated structures. Earthquake Engng Struct Dyn 2011;40:1629–51.
[23] Dang Y, Han J, Li Y. Analysis of the seismic performance of ısolated buildings according to life-cycle cost. Comput. Intell. Neurosci. 2015. Article ID 495042.
[24] Pinto PE, Vanzi I. Base-isolation: reliability for different design criteria. Earthquake engineering tenth world conference, Rotterdam 1992:2033–8.
[25] Takeda M, Ohkawa Y, Akutsu Y. An evaluation method for seismic isolation effect in siting of a nuclear facility. Reliab Eng Syst Saf 1998;62:241–9.
[26] De Grandis S, Domaneschi M, Perotti F. A numerical procedure for computing the fragility of NPP components under random seismic excitation. Nucl Eng Des 2009;239:2491–9.
[27] Fan J, Zhang Y. A hybrid probability-convex model for the seismic demand analysis of bearing displacement in the benchmark base-isolated structure. Adv Struct Eng 2014;17(7):1061–73.
[28] Castaldo P, Amendola G, Palazzo B. Effects of class B site on the seismic reliability of base-isolated steel systems. Ingegneria Sismica 2016;33(3):29–41.
[29] Castaldo P, Palazzo B, Ferrentino T. Seismic reliability-based ductility demand evaluation for inelastic base-isolated structures with friction pendulum devices. Earthquake Engng Struct Dyn 2017;46:1245–66.
[30] Moeindarbari H, Taghikhany T. Seismic reliability assessment of base-isolated structures using artificial neural network: operation failure of sensitive equipment. Earthquakes Struct. 2018;14(5):425–36.
[31] Nagarajaiah S, Reinhorn AM, Constantinou MC. 3D-BASIS: a general program for the nonlinear dynamic analysis of three dimensional base isolated buildings. New York, USA: National Center for Earthquake Engineering Research, State University of New York at Buffalo; 1991.
[32] Gazi H. Probabilistic behavior of seismically isolated buildings under earthquake loadings. Istanbul, Turkey: Istanbul University; 2015. PhD dissertation.
[33] Tena-Colunga A, Escamilla-Cruz JL. Torsional amplifications in asymmetric base-isolated structures. Eng Struct 2007;29:237–47.
[34] SAP2000. Integrated Software for Structural Analysis and Design, Computers and Structures Inc., USA; 2016.
[35] Nagarajaiah S, Reinhorn AM, Constantinou MC. Nonlinear dynamic analysis of three-dimensional base isolated structures (3D-BASIS): Technical report NCEER-89-0019, National Center for Earthquake Engineering Research, State University of New York, Buffalo; 1989.
[36] Makris N. Rigidity, plasticity, viscosity: can electrorheological dampers protect base isolated structures from near source ground motions? Earthquake Eng Struct Dyn 1997;26:571–91.
[37] Building Center of Japan. Report on new building technologies – approvals, appraisals and certification. Technical Report of the Building Center of Japan; 2002. p. 75–82.
[38] ASCE/SEI 41-13. Seismic evaluation and retrofit of existing buildings. American Society of Civil Engineers, Reston, Virginia, ISBN: 978-0-7844-7791-5; 2014.
[39] Pan P, Ye LP, Shi W, Cao HY. Engineering practice of seismic isolation and energy dissipation structures in China. Sci. China – Technol. Sci. 2012;55(11):3036–46.
[40] Bridgestone. Seismic isolation product line-up, Bridgestone Corporation – Infrastructure Products Business Development Department, Tokyo 103-0028, Japan; 2015.
[41] Ryan KL, Chopra AK. Estimation of seismic demands on isolators based on nonlinear analysis. J Struct Eng 2004;130(3):392–402.
[42] Ryan KL, Earl CL. Analysis and design of inter-story isolation systems with nonlinear devices. J Earthquake Eng 2010;14:1044–62.
[43] Sharma A, Jangid RS. Influence of high initial isolator stiffness on the seismic response of a base-isolated benchmark building. Int J Struct Stab Dyn 2011;11(06):1201–28.
[44] Naeim F, Kelly JM. Design of seismic isolated structures from theory to practice. New York: Wiley; 1999.
[45] DIS. Seismic isolation for buildings and bridges. Dynamic Isolation Systems Inc., Nevada 89434, USA; 2007.
[46] Nowak AS, Collins KR. Reliability of structures. Boston: Mc Graw-Hill Companies Inc.; 2000.
[47] Kastner M. Monte Carlo methods in statistical physics: mathematical foundations and strategies. Commun Nonlinear Sci Numer Simul 2010;15(6):1589–602.
[48] Alhan C, Gazi H. Bringing probabilistic analysis perspective into structural engineering education: use of Monte Carlo simulations. Int J EngEduc 2014;30(5):1280–94.
[49] Castelnuovo E. Monetary policy shocks and financial conditions: a Monte Carlo experiment. J Int Money Finance 2013;32:282–303.
[50] Wang Z, Wang Y, Ma M, Wu J. Efficient localization for mobile sensor networks based on constraint rules optimized Monte Carlo method. Comput Netw 2013;57(14):2788–801.
[51] Haldar A, Mahadevan S. Probability reliability and statistical methods in engineering design. Danvers MA: John Wiley and Sons; 2000.
[52] Bray JD, Marek AR. Characterization of forward-directivity ground motions in the near-fault region. Soil Dyn Earthquake Eng 2004;24:815–28.
[53] Somerville P, Engineering characterization of near fault ground motions. In: Planning and engineering for performance in earthquakes (2005 NZSEE), New Zealand; 2005.
[54] Malhotra PK. Response of buildings to near-field pulse-like ground motions. Earthquake Eng Struct Dyn 1999;28:1309–26.
[55] Sehhati R, Rodriguez-Marek A, Elgawady M, Cofer WF. Effect of near-fault ground motions and equivalent pulses on multi-story structures. Eng Struct 2011;33:767–79.
[56] Shoaei P, Orimi HT, Zahrai SM. Seismic reliability-based design of inelastic base-isolated structures with lead-rubber bearing systems. Soil Dyn. Earthquake Eng. 2018;115:589–605.
[57] Castaldo P, Palazzo B, Alfano G, Palumbo MF. Seismic reliability-based ductility demand for hardening and softening structures isolated by friction pendulum bearings. Struct Control Health Monit 2018;25.
[58] PEER. Pacific Earthquake Engineering Resource Center: NGA Database; 2018. < http://ngawest2.berkeley.edu/ > .
[59] De la Llera JC, Luders C, Leigh P, et al. Analysis, testing, and implementation of seismic isolation of buildings in Chile. Earthquake Eng Struct Dyn 2004;33(5):543–74.
[60] Providakis CP. Effect of LRB isolators and supplemental viscous dampers on seismic isolated buildings under near-fault excitations. Eng Struct 2008;30(5):1187–98.
[61] Gazi H, Öncü Davas S, Alhan C. Comparison of ground motion pulse models for the drift response of seismically isolated buildings. In: Urban Planning and Civil Engineering, Virginia P. Sisiopiku, Ossama E. Ramadan, editors. Athens Institute for Education and Research, Athens; 2015. p. 321–32.
[62] Mizuno H, Iiba M, Yamaguchi N. Earthquake resistance of medical equipments with casters. In: Proceedings of the 7th Japanese earthquake engineering symposium, Tokyo, Japan; 1986. p. 1837–42.
[63] WorkSafe Technologies. Effects of seismic vibrations on disk drives; 2013. < http://www.worksafetech.com/pages/isotest.html > [accessed: April, 2013].
[64] Architectural Institute of Japan. Recommendation for the design of base isolated structures, Japan; 2001.
[65] Alhan C, Sahin F. Protecting vibration-sensitive contents: an investigation of floor accelerations in seismically isolated buildings. Bull Earthq Eng 2011;9:1203–26.